



UNIVERSITÀ
DEGLI STUDI
DI TRIESTE

Dipartimento di Fisica

CORSO DI LAUREA MAGISTRALE
INTERATENEO IN FISICA

Curriculum Fisica nucleare e subnucleare

TESI DI LAUREA MAGISTRALE

Studio di un modello fisico dei blip e altri glitch
negli interferometri di onde gravitazionali

Laureando:
Fabrizio Diaz Guerra

Relatore:
Prof. Edoardo Milotti

Correlatore:
Dott.ssa Agata Trovato

Abstract

In questo lavoro di tesi viene affrontato uno degli argomenti di punta nello studio dei segnali provenienti dagli interferometri che ricercano onde gravitazionali: i glitch. Questa tipologia di eventi, tipicamente di origine strumentale e di breve durata, contamina le misure finendo spesso per confondersi o sovrapporsi agli eventi di origine astrofisica che invece si vanno a ricercare.

In questa tesi verrà studiata un'ipotesi sull'origine di alcune tipologie di glitch: il rumore Barkhausen. Questo fenomeno, la cui spiegazione trova origine nella teoria della materia condensata, si verifica nei materiali ferromagnetici e introduce delle fluttuazioni nella loro curva di magnetizzazione. Le microscopiche deviazioni casuali dall'andamento ideale che possono originarsi in alcune parti dell'apparato di misura, come gli attuatori elettromagnetici, diventano quindi delle forze che si propagano negli apparati di misura e, grazie all'eccezionale sensibilità dei detector, vengono registrate competendo con i segnali reali.

Gli impulsi vengono simulati con dei cammini casuali di Lévy, in un modello a due parametri. Le camminate vengono immerse in campioni di fondo di rumore Gaussiano, con le stesse caratteristiche di quello dei rivelatori. I segnali così ottenuti possono essere trattati allo stesso modo dei glitch reali, e quindi confrontati e classificati con modalità che ricalcano quelle standard. Dai segnali dei glitch generati vengono misurate delle grandezze specificatamente individuate per questa tipologia di segnali, le cui distribuzioni vengono studiate. Con queste viene costruita una procedura in grado di inferire i parametri del modello da un set ridotto di glitch.

Una volta trattati i glitch isolati, l'attenzione viene spostata sui meccanismi che regolano la loro comparsa. In particolare viene costruito un modello che consenta di riprodurre il loro caratteristico andamento nel tempo: spesso appaiono a piccoli gruppi separati da lunghi periodi di quiete.

Un modo sistematico di generare questi treni di impulsi viene quindi implementato e sfruttato per stimare il contributo che questo tipo di eventi può portare all'ampiezza spettrale media di rumore, trovando un andamento proporzionale all'inverso della frequenza.

Contents

1	Introduction	1
1.1	Interferometers of the LVK collaboration	1
1.1.1	Gravitational waves	1
1.1.2	Detector layout	2
1.1.3	The challenge of noise reduction	2
1.1.4	Electromagnetic components	4
1.2	Observed detector noise	5
1.2.1	The colored stationary Gaussian noise background	5
1.2.2	Glitches	7
1.2.3	Clues to a model	8
1.3	The Barkhausen noise	9
1.3.1	Magnetism in materials	9
1.3.2	Anisotropies and hysteresis	11
1.3.3	Magnetic walls and their dynamic	13
1.3.4	Barkhausen noise	14
1.3.5	Barkhausen noise as crackling noise	16
1.3.6	Random walkers	17
1.4	Glitch occurrence	19
1.4.1	Bursts and intermittency	19
1.4.2	Dissipative dynamical systems	19
2	Know your glitches	23
2.1	Method	23
2.1.1	Glitch generation	23
2.1.2	Glitch identification	25
2.1.3	Glitch analysis	28
2.2	Observations	31
2.2.1	Glitch morphology	31
2.2.2	Glitches in other spaces	33
2.2.3	Glitch quantities	34
2.3	Finding the parameters	36
2.3.1	Likelihood of a quantity	36
2.3.2	Glitches discrimination	37
2.3.3	Computing the likelihood	38
2.3.4	Estimation tests	38
3	Waiting for a glitch	45
3.1	Waiting times	45
3.1.1	Implementation	45
3.1.2	Parameters of the bursts model	45
3.1.3	Glitch probability	47
3.1.4	Waiting times shapes	47
3.2	Spectral modification	50
3.2.1	Glitch injection	50

3.2.2	Windowing	51
3.2.3	Spectral modification	51
4	Conclusions and future prospects	55
	Bibliography	57

Introduction

1.1 Interferometers of the LVK collaboration

In this thesis, I study a class of disturbances affecting the data streams of the gravitational interferometers of the LIGO-Virgo-KAGRA Collaboration. These detectors are extremely advanced and can measure relative length changes of the order of 10^{-20} , and must be carefully shielded from all kinds of environmental and instrumental noises.

At the time of this writing, it has been almost ten years since the first direct detection of a gravitational wave [1], and since then the sensitivity of the interferometers increased considerably. The upgrades have led to a reduced impact of all noise sources, and research in this field continues with a push to higher and higher sensitivities.

1.1.1 Gravitational waves

Here, I do not provide an account of the theory of gravitational waves except for a very schematic description (see, e.g., [2] for an extended description). In the standard description, i.e., in the comoving TT-gauge, gravitational waves are transverse waves with two distinct polarization states. A gravitational wave in the *plus polarization* produces simultaneous stresses with opposite signs along orthogonal axes while the *cross polarization* would produce the same deformation pattern along a frame with a 45° rotation.

Since the gravitational force is weak in a terrestrial environment, the generation of detectable gravitational waves in a laboratory is a practical impossibility, but there are many powerful astrophysical sources of gravitational waves such as pairs of gravitationally

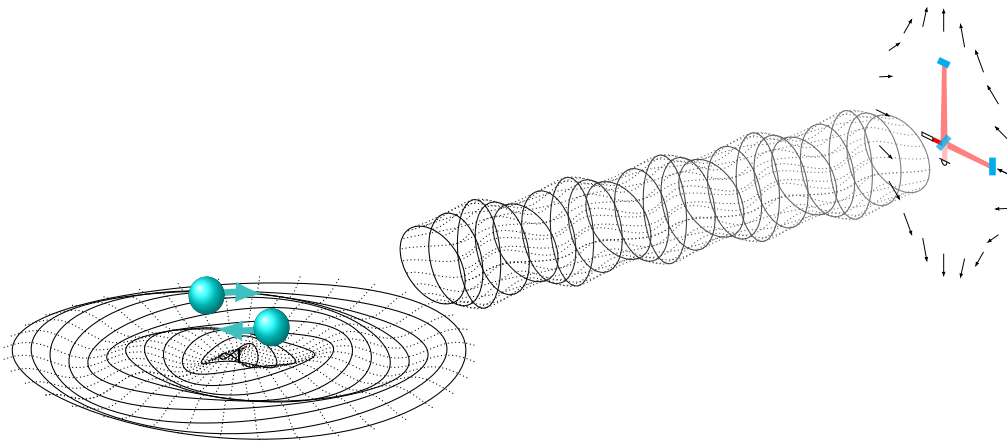


Figure 1.1: Gravitational wave generation, propagation, and detection. A source (in this case, the merger of a pair of compact objects) produces gravitational waves. They propagate in spacetime, and reach an interferometer. The differential change in arm length is detected as a change in the interference pattern in the Michelson-type interferometer.

bound compact objects, stellar collapses with an imperfect spherical symmetry, and cosmological events in the early universe. Although the radiated power can be huge, these objects are quite distant and the strains due to the gravitational waves reaching the Earth are barely detectable.

1.1.2 Detector layout

Current gravitational-wave interferometers are based on the Michelson interferometer structure [3], where a laser beam is split by a semi-reflecting mirror (the beam splitter), and the resulting beams are then back-reflected by two end mirrors (see figure 1.2a). These reflected beams recombine and split again at the beam splitter, where one of the outgoing beams returns to the laser source and the other one reaches a photodiode. The two half-beams that reach the photodiode carry with them the spatial phase accumulated on the back and forth journeys along the two arms and interfere at the the photodiode. The interference pattern changes if the arms are stretched/compressed by a gravitational wave and the photodiode records the changing intensity of the interference pattern.

In practice, this very elementary scheme must be supplemented by many upgrades. For instance, each end mirror in the interferometer arms is replaced by a Fabry–Perot cavity with slightly different mirrors, so that it acts as a single mirror with a reflectivity that is modulated by any change in the spatial distance of the cavity mirrors, and is amplified by the finesse of the cavity.

Overall, each interferometer is an extremely complex optical instrument. A measure of its complexity is given by the large number of sensors used to monitor its behavior, which is of the order of 250 000.

1.1.3 The challenge of noise reduction

Because of the extreme weakness of gravitational–wave signals, beating noise is an important challenge confronting scientists. The main types of noise affecting gravitational–wave interferometers are

quantum noise due the particle nature of light, there are statistical fluctuations over the number of photons that are revealed by the photodiode, but also there is a discontinuous radiation pressure applied to the mirrors;

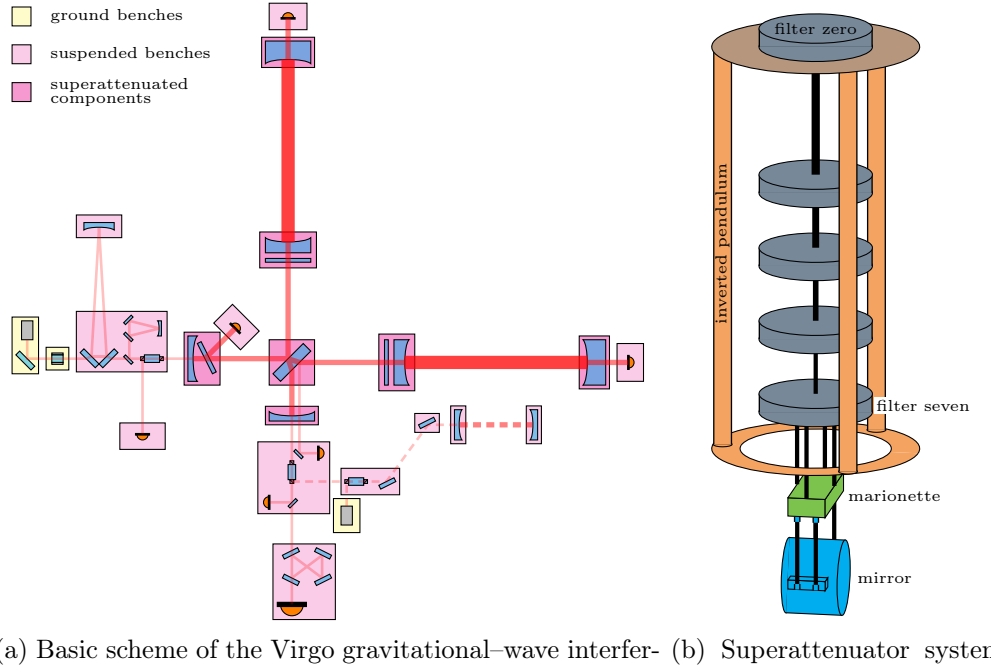
seismic noise vibrations at low frequencies of the terrain where the detector is built, counteracted by the suspensions systems;

gravity gradients Newtonian attraction with surrounding objects, measured with sensors around the test masses;

suspension thermal noise small vibrations of the suspension system material, reduced with monolithic fused silica suspensions;

mirror thermal noise small distortions and vibrations in the materials that form the mirrors, reduced by studying and finding better materials for the mirror coatings;

1.1. INTERFEROMETERS OF THE LVK COLLABORATION



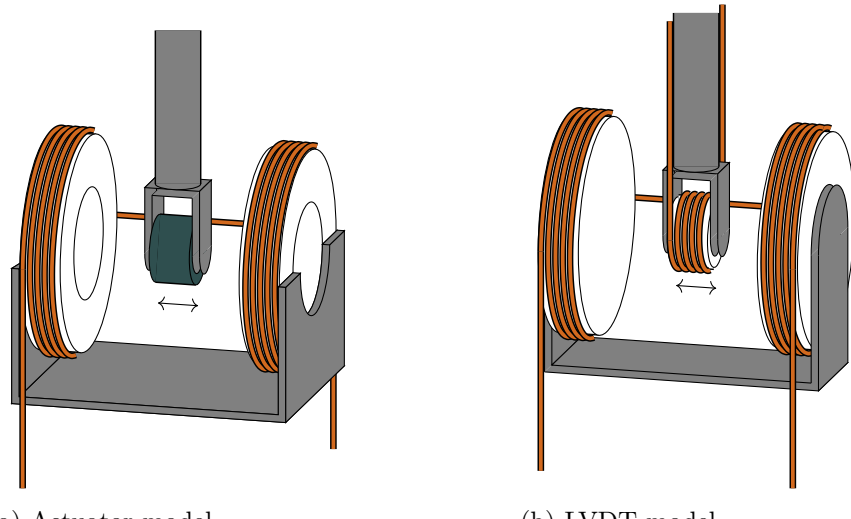
(a) Basic scheme of the Virgo gravitational-wave interferometer.
(b) Superattenuator system at Virgo.

Figure 1.2: Left panel: basic scheme of the Virgo gravitational-wave interferometer. Right panel: sketch of a Virgo *superattenuator*; the superattenuators are suspension systems designed to minimize seismic noise and environmental vibrations. Each superattenuator in Virgo includes 23 electromagnetic actuators and 18 LVDTs [4]. Many more such components are used elsewhere in the instrument.

excess gas light scattering due to the residual gas present in the device.

As an example of a subsystem dedicated to minimizing and controlling seismic noise and environmental vibrations, I focus on the Virgo superattenuators (see figure 1.2) [5, 6].

Superattenuators are used for the main components of the interferometer. They support the end mirrors, the beam splitter, and the recycling mirrors. Basically, they are inverted pendulums with many intermediate stages and ending with a final stage called *marionette*. The inverted pendulum consists of three legs with lengths exceeding six meters. At the top, there is the first stage of suspension: the zero filter. The following stages hang from it, each one tuned to resonate at a certain frequency. Their mechanisms absorb vibrations at almost every frequency above 10 Hz creating a stable support. Each stage is composed by a large mass, suspended at its center of mass by a steel wire. The next stage is connected to a crossbar, which is attached to the stage body by many *blades*. These are triangular sheets of metal that act as springs. To soften their elasticity there is a system of magnetic anti-springs around the crossbar. The exact positions at stage zero



(a) Actuator model.

(b) LVDT model.

Figure 1.3: Drawing of two electromagnetic components used to control the filter zero at Virgo [6]. The LVDTs are sensors that measure small linear displacements, the actuators try to compensate unwanted movements with magnetic elements.

and seven are monitored and regulated by sensors, motors and actuators, which make sure that the alignment alignment of the system is correct. The last stage, filter seven, is attached to the *marionette* by a system made of springs and actuators. The mirrors are attached to the marionette by fused silica wires, to minimize thermal fluctuations.

The interferometer also includes standard suspension systems which are shorter, as they have only the first and the last stages used in the superattenuators and are used for optical benches or smaller mirrors.

1.1.4 Electromagnetic components

Many parts of the suspension systems have electromagnetic components that are used to control the positions of all the elements. There are three types of electromagnetic components:

- **Linear Variable Displacement Transducer (LVDT)** elements composed by three coils that measure linear displacements between two objects (see figure 1.3)
- **motors** active elements that move part of the system
- **coil-magnet actuators** active elements that apply a force between two objects, to fine tune their distance (see figure 1.3).

Most of these components are part of feedback loops that maintain the system aligned.

The electromagnetic actuators are a simple kind of electrical devices: they use the controlled magnetic field produced by a coil to move a magnet. There are 23 such coils in every superattenuator, to control all the degrees of freedom of important parts of the system. Some of them are included in the first and last stages of the filters, some are on the marionette itself, while others are glued on mirrors.

Virgo LVDTs [7] are a specific kind of sensors: the middle coil is powered with alternate current to produce a variable magnetic field. The adjacent coils belong to the same circuit and are identical but wound in opposite directions so that the induced potential voltage cancels out. When the middle coil is displaced, the voltages are unbalanced and the circuit produces a feedback signal (the sign of the feedback signal indicates the direction of the displacement). There are 18 LVDT sensors monitoring the alignments of the components of each superattenuator. Finally, the stepper motors are used for fine adjustments. We shall see that the pervasive presence of electromagnetic components in the detectors may be a source of unwanted signals that plague measurements. These unwanted signals are a manifestation of a complex chaotic dynamics and as such they are akin to noise.

1.2 Observed detector noise

In this section, I briefly discuss the observed noise which — over short stretches of time — can be classified as a colored stationary Gaussian background plus a complex non-Gaussian population of short transients.

1.2.1 The colored stationary Gaussian noise background

The sources identified in section 1.1.3 are all expected to produce colored Gaussian noise, and overall the measured shape of the noise amplitude spectral density (ASD) appears as show in figure 1.4, which can be explained as the sum of the ASDs of many individual noise sources (see [8] for a more complete list of the individual noise components). Measurements of the power spectral density (PSD) are carried out by averaging over many time slices [9].

In addition to noise, the ASDs also show the presence of fairly well-defined spectral lines that originate from mechanical oscillations of the quartz fibers in the suspension systems and other mechanical parts. When combined with noise, these lines lead to signal fluctuations that are orders of magnitude larger than the expected gravitational-wave signals. For this reason, the raw output of the photodiode must be *whitened* [10]. The whitening procedure consists in 1) estimating the ASD as explained above, 2) computing the Fourier transform $\tilde{h}(f)$ of the measured photodiode output (called $h(t)$), 3) dividing $\tilde{h}(f)$ by the the noise ASD, 4) transforming back to the time domain to obtain the

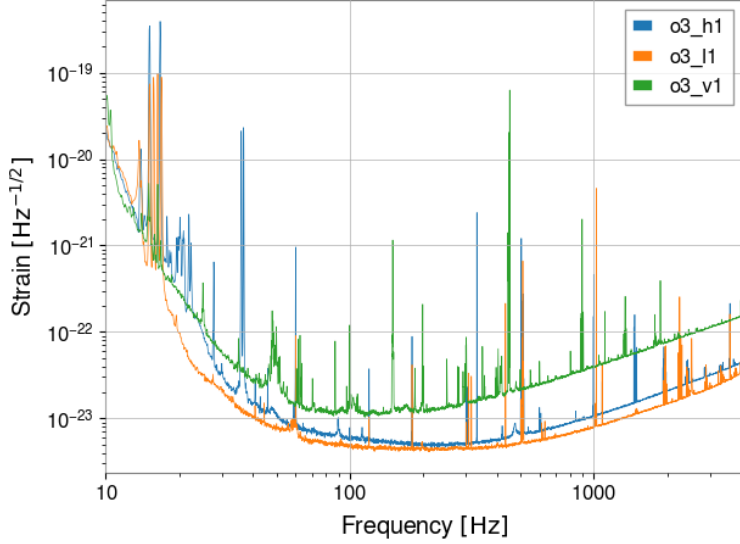


Figure 1.4: Amplitude spectral density of noise for the detectors of the LVK Collaboration in the O3 observing run (h1: LIGO Hanford; l1: LIGO Livingston; v1: Virgo).

whitened signal $w(t)$

$$h(t) \xrightarrow{\text{DFT}} \tilde{h}(f) \xrightarrow{\text{whitening}} \tilde{w}(f) = \frac{\tilde{h}(f)}{\sqrt{S_n(f)}} \xrightarrow{\text{IDFT}} w(t) = \mathcal{F}^{-1} \left(\frac{\tilde{h}(f)}{\sqrt{S_n(f)}} \right) \quad (1.1)$$

In the case of an ideal colored Gaussian background, this procedure transforms the measured $h(t)$ into a white Gaussian noise with unit variance.

If $h(t)$ represents a real gravitational signal, we define an important quantity, the signal-to-noise ratio (SNR), as follows:

$$\rho^2 = 4 \int_0^\infty \frac{|\tilde{h}(f)|^2}{S_n(f)} df \quad (1.2)$$

Below, we shall see that it quite useful to simulate colored Gaussian noises, and to this end I use the simple algorithm proposed by J. Timmer and M. König [11]. Basically, for an n -sample real time series, we only need to compute $n_{\text{Nyquist}} = n/2 + 1$ complex coefficients. In the case of Gaussian noise, each complex coefficient is a complex random variable with Gaussian real and imaginary part. Thus, for every frequency, except the first and the last, two random normal values are drawn to obtain:

$$\tilde{h}(f_i \neq f_0, f_{\text{Nyquist}}) = (\mathcal{N}(0, 1) + i\mathcal{N}(0, 1)) \times \sqrt{\frac{S_n(f_i)}{2}}$$

1.2. OBSERVED DETECTOR NOISE

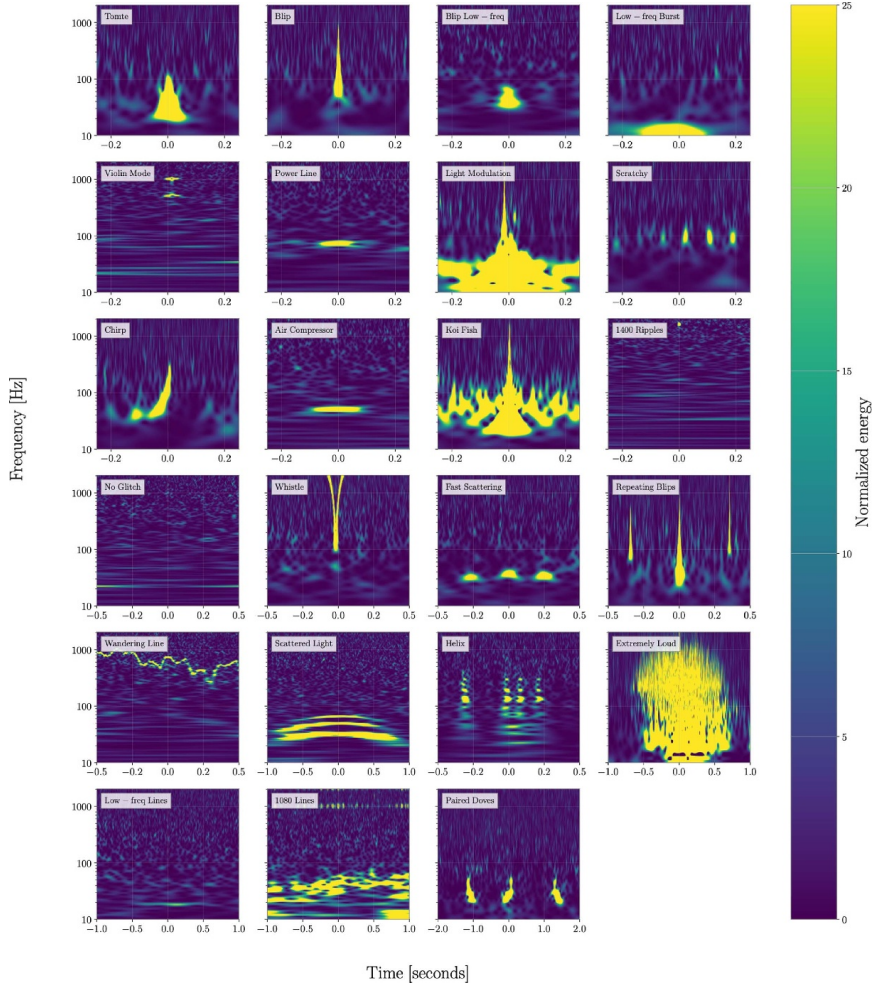


Figure 1.5: Classes of glitches reported by Gravity Spy [12].

while for the first and last generated frequencies only the real component are drawn, since the symmetries of the spectrum of a real signals require a null imaginary component. Once all the frequency values are generated, an inverse Fourier transform is applied to obtain the corresponding time signal.

1.2.2 Glitches

The non-Gaussian component of noise is mostly associated with short transients called *glitches*. These short transients are a particularly annoying disturbance because they can mimic some gravitational-wave signals and display a wide variety of shapes in the time domain and in the time-frequency domain. We obtain time-frequency representations of $h(t)$ with different techniques which range from simple spectrograms, which are based on the short-time Fourier transform to the wide selection of discrete and continuous

wavelets, and to the Q-transform [10]. Just as standard spectrograms, the Q-transforms are simple and powerful tools that are used to study the spectral composition of a signal over time. The Q-transform is defined as follows:

$$x(t, f) = \int_{-\infty}^{\infty} x(t') w(t' - t, f) e^{-i2\pi ft'} dt' \quad (1.3)$$

where the window function $w(t, f)$ depends on frequency and on the Q parameter. Higher values of Q produce wider time windows and thus a lower time resolution, but have a larger frequency resolution. The standard algorithm used to represent events in the time-frequency domain uses a maximization method to select an optimal Q value.

Using the Q-transform to represent glitches in the time-frequency domain, we note that there are recurring shapes. This observation has started the classification of glitches, standardized by the Gravity Spy project [12]. The goal of this project is to classify as many glitches as possible, creating a catalog of glitches.

Initially, the glitches were categorized in classes with fancy names like *blip*, *koi fish* and many more, by the scientists who studied this phenomenon. These categories were based only on the glitch appearance: if the Q-scans of two glitches seemed different, they were put in different categories. As the classification proceeded, some other classes were added and some existing classes were merged together, leaving us with 23 glitch classes.

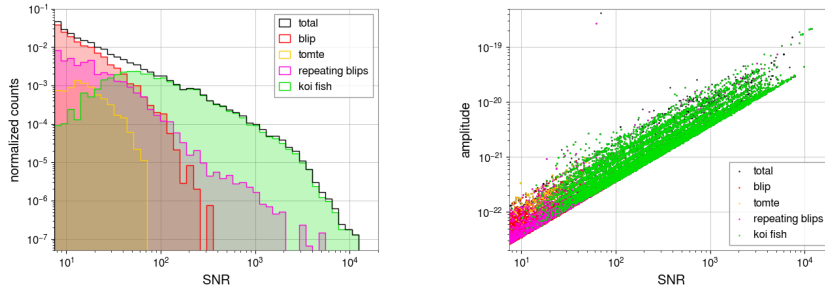
Gravity Spy is a citizen science project and the classification of new glitches receives an important input from volunteers who join remotely the project and whose work is supervised by scientist of the Gravity Spy community. In this way, numerous glitches are classified, generating a training set for a specialized neural network. The neural network then learns from the classification produced by the volunteers, and is ready to classify a stream of new glitches. For every new glitch, the neural network outputs the probability that it belongs to one of the known categories.

To standardize the procedure, the color palette of the Q-scans is set to a maximum value of 25 (in units of standard deviation of the whitened noise). With the selected Q-scan parameters, some small glitches can just fade in the background. Overall, only glitches with an SNR larger than 7.5 are processed. The origin of some glitch classes have been discovered, but many of them are still mysterious.

1.2.3 Clues to a model

Recently, the Gravity Spy team has published a catalog of glitches with many associated quantities characterizing them [12]. Some of them come from the identification process, such as the event time or the identification confidence, and others from the pipeline that searches for events: the Omicron pipeline [13].

By selecting glitches belonging to specified classes, like *blip*, *tomte* and *koi fish*, with a probability larger than a certain threshold (in our case 90%), we can study the distribution of their associated Omicron quantities. We often find that different classes share



(a) The SNR distribution among some classes of glitches and a total distribution. We can see how the distributions complete each other.

(b) A scatter plot of amplitude and SNR for the same glitches, where we can observe a linear dependence of those quantities.

Figure 1.6: Distribution of some quantities from the Gravity Spy glitch database [12]. In these examples we can see some properties that the glitches have, so those are the request that a model must cover.

common trends. An example is the SNR distribution in Fig. 1.6a where small values are dominated by a power-law distribution from the *blips*, while for larger value this trend is continued by the higher SNR *koi fish*. If we plot the two distributions together, we see that they combine to produce a power law that covers at least two orders of magnitude. This suggests studying all glitches from these categories together, as if they originated from the same source. I checked that this result was not an artifact due to the specific threshold, taking different values, 99%, 95%, 90%, 75%, but the results did not change. We also observe a linear dependence of pairs of quantities, like integrated SNR and amplitude, as in Fig. 1.6b. This suggests that the process that generates this kind of events has a certain regularity. In this specific case, the shape of the signal appears to be correlated with the signal amplitude, and this suggests a scale invariance of the signal shape.

1.3 The Barkhausen noise

The data presented in the previous section point to a known class of phenomena characterized by multiple power–law noises, the *crackling noises*. A specific kind of crackling noise, the Barkhausen noise, is the candidate that I study in this thesis as possible source of some glitch classes.

1.3.1 Magnetism in materials

From antiquity, we know that some materials can interact with magnetic fields. There are three fundamental classes of materials, based on the interaction they have with a magnet:

- **diamagnetic** materials, where the material is slightly repelled by a magnet;
- **paramagnetic** materials, where there is a slight attraction between the sample and a magnet;
- **ferromagnetic** materials, are the materials with the strongest interaction with a magnet, so much that they can become magnets themselves.

The magnetic properties of a material originate in the spin pairings of the electrons in the material [14].

To a first approximation we can describe the electron path as a circular trajectory around the nucleus. The electron continuous motion can be seen as a local electrical current, so the net result from every electron is that we have a constant current in a circular loop. This originates a small magnetic field, as we know from the coils electromagnets working principle. The small electromagnetic field takes the shape of a magnetic dipole. Its entity is bound to the classical angular momentum of the electron with the relation $\mu = \frac{e\hbar}{2m_e} \mathbf{L}$. The angular momentum of an electron when it stays in an atomic orbital is predicted to be dependent from the corresponding quantum number l by the relation $L = \hbar\sqrt{l(l+1)}$ so the magnetic momentum of an electron in an atom can be written as:

$$\|\boldsymbol{\mu}\| = \frac{e\hbar}{2m_e} \sqrt{l(l+1)}$$

Since an electron also has a spin, we have to take in account the total angular momentum j instead of only the orbital momentum l or the atomic spin S :

$$\|\boldsymbol{\mu}\| = \frac{e\hbar}{2m_e} \sqrt{j(j+1)} = \mu_B S \quad (1.4)$$

The contribution from the magnetic dipole of every electron in an atom tends to cancel out, so there is no net magnetic momentum in an atom, unless there are unpaired electrons. Ferromagnetic materials have unpaired electrons, so every atom behaves like a magnetic dipole.

The field that comes from all the magnetic dipoles in the material is called magnetization field, and is defined as:

$$\mathbf{M} = \sum_i \frac{1}{4\pi} \left(\frac{3\mathbf{r}_i \boldsymbol{\mu}_i \cdot \mathbf{r}_i}{r_i^5} - \frac{\boldsymbol{\mu}_i}{r_i^3} \right) = \sum_i \mathbf{f}(\mathbf{r}_i, \boldsymbol{\mu}_i) \quad (1.5)$$

that is relevant only at short distance. In fact, in ferromagnetic materials the atoms are so packed that everyone of them can sense the magnetic field from its neighbors.

The energy that a magnetic dipole $\boldsymbol{\mu}_j$ has while in a magnetic field \mathbf{B} can be expressed with the Hamiltonian:

$$H = \sum_j -\boldsymbol{\mu}_j \cdot \mathbf{B}$$

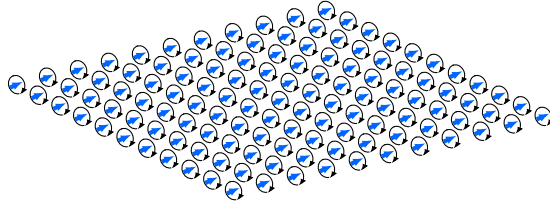


Figure 1.7: Atomic dipoles from unpaired electrons in a ferromagnetic material. Here the atomic dipoles generated by unpaired electrons are represented.

Where the field \mathbf{B} accounts both external fields \mathbf{H} and internal fields \mathbf{M} . So, the last term can be expanded from the contribution of all the other magnetic dipoles in the material:

$$H = \sum_j -\boldsymbol{\mu}_j \cdot \mu_0 \left(\mathbf{H} + \sum_i \mathbf{f}(\mathbf{r}_i, \boldsymbol{\mu}_i) \right) = \sum_{i,j} -\mu_0 \boldsymbol{\mu}_j \cdot \mathbf{f}(\mathbf{r}_i, \boldsymbol{\mu}_i) + \sum_j -\mu_0 \boldsymbol{\mu}_j \cdot \mathbf{H}$$

We can rewrite the equation using some constants that account for the scalar products, so the resulting Hamiltonian can be written as:

$$H = \sum_{i,j} -J_{ij} \boldsymbol{\mu}_j \cdot \boldsymbol{\mu}_i + \sum_j -J_i \boldsymbol{\mu}_j \cdot \mathbf{H}$$

from where we can extract the contribution for a single atom:

$$H_j = -\boldsymbol{\mu}_j \cdot \left(\sum_i J_{ij} \boldsymbol{\mu}_i + \mathbf{H} \right) \quad (1.6)$$

In this equation we can note that the energy is influenced from both the external field, but also from the neighbors of the atom.

In a ferromagnetic material, the minimum energy is reached when the atomic dipoles align themselves in the same direction of the surrounding ones. This creates a region of material where all the atomic dipole are aligned. A region of this kind is called a magnetic domain.

Inside a piece of ferromagnetic materials there are thousands of magnetic domains, and every one is aligned to a different direction. Thus, the total mean magnetization of the material can be zero, even if every domain has its own local strong field.

1.3.2 Anisotropies and hysteresis

In a crystalline structure, not all directions work the same way. There can be some preferred and some disfavored directions, even for magnetism. Those directions are called

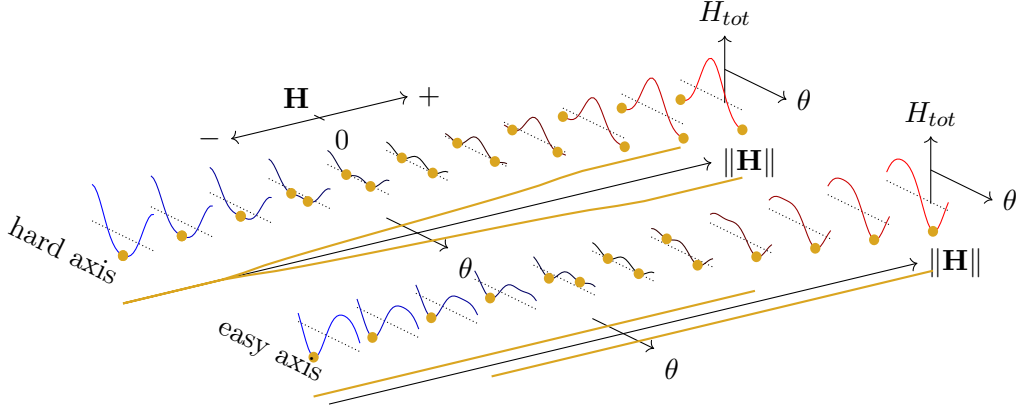


Figure 1.8: Energy of a single domain in function of the angle between its magnetization field and the easy axis of the material and the external field intensity. In the case of an external field oriented as a hard axis, the system can smoothly follow the field. In the case of the easy axis, the system must jump to one solution to another.

respectively the easy and the hard axis. This introduces an anisotropy in the behavior of a magnetization model.

We can analyze a simple case, with a unique magnetic domain and a single easy axis. The external field is also in the same plane of the magnetization field and the easy axis. The presence of a preferred axis of magnetization can be formulated with an anisotropic energy:

$$H_a = K_a \sin^2(\theta) \quad (1.7)$$

where θ is the angle between the easy axis and the magnetization field. The energy of the system, when we add an external field is now:

$$H_{tot} = K_a \sin^2(\theta) + HM \cos(\phi - \theta) \quad (1.8)$$

with ϕ the angle between the external field and the easy axis.

We can study how the system responds to the external field finding the direction of the magnetization field as the energy minima in two particular cases: when the external field goes perpendicular or in the same direction of the easy axis.

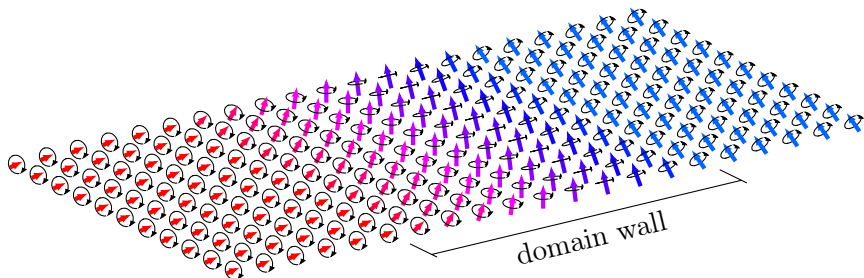
In the first case, with $\phi = \pm\pi$, we find that:

$$0 = \frac{dH_{tot}}{d\theta} = 2K_a \sin(\theta) \cos(\theta) + HM \cos(\theta) \Rightarrow \theta = \arcsin\left(-\frac{HM}{2K_a}\right)$$

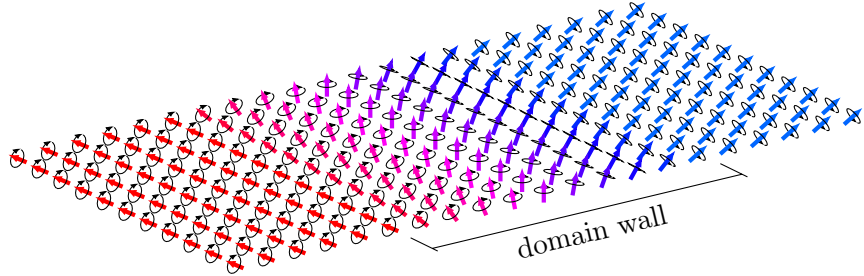
So the magnetization field slowly aligns to the external field, as its intensity increase.

In the second case, with $\phi = 0, \pi$ the minima are:

$$0 = \frac{dH_{tot}}{d\theta} = 2K_a \sin(\theta) \cos(\theta) \mp HM \sin(\theta) \Rightarrow \theta = 0, \pi$$



(a) A Bloch wall.



(b) A Néel wall.

Figure 1.9: Different kinds of walls. In Bloch walls the variation of the dipole direction happens in a plane parallel to the wall. In Néel walls the plane is perpendicular to the wall.

We can see that there is no continuity from one solution to another, so the system must jump from the easy axis to be aligned with the external field.

The two cases are illustrated in 1.8.

With more easy axis and different planes for the two angles the solutions share the same principles, but the mathematic behind them is more complicated.

The solution we have found can explain how the hysteresis phenomena originates: in a ferromagnetic material we have some stable solutions where the system sits, and these solutions slowly becomes unstable when an external field varies, so the system make many jumps to adjust itself.

1.3.3 Magnetic walls and their dynamic

The regions between two magnetic domains are called magnetic walls. In these regions, the direction of atomic dipoles make a smooth transition from the common alignments of the domains. Some examples of walls are shown in Fig. 1.9.

Let γ be the angle between the directions of dipole momentum in the two domains separated by a wall. If it is n atoms thick, the angle between two adjacent dipoles will

be $\delta\gamma = \frac{\gamma}{N}$. For every dipole, the energetic contribution with its neighbors comes from the first term in Eq. 1.6:

$$H_{ij} = -J_{ij}\boldsymbol{\mu}_i \cdot \boldsymbol{\mu}_j = -J_{ij}\|\boldsymbol{\mu}\|^2 \cos\left(\frac{\gamma}{N}\right) \simeq -J_{ij}\|\boldsymbol{\mu}\|^2 \left(1 - \frac{\gamma^2}{2N^2}\right)$$

The total energy from the wall is obtained accounting also the anisotropic contribution from Eq. 1.7 for every atom. Since in the magnetic domains the atoms are aligned with their easy axis, the angle θ for the i -th atom simply assumes the value $i\delta\gamma$. The energy of the wall is then:

$$H_{a,\text{wall}} = \sum_i^N K_a \sin^2(i\delta\gamma) = \frac{NK_a}{2}$$

So the total energy of the wall is:

$$H_{\text{wall}} = H_{a,\text{wall}} + NH_i \simeq \frac{NK_a}{2} - J_{ij}\|\boldsymbol{\mu}\|^2 \left(N - \frac{\gamma^2}{2N}\right)$$

The optimal thickness in terms of number of atom can be found minimizing the energy:

$$0 = \frac{dH_{\text{wall}}}{dN} \simeq \frac{K_a}{2} - J_{ij}\|\boldsymbol{\mu}\|^2 \left(1 + \frac{\gamma^2}{N^2}\right) \Rightarrow N = \gamma\|\boldsymbol{\mu}\| \sqrt{\frac{2J_{ij}}{K_a}} \quad (1.9)$$

This equation tells us that thicker walls can be found in materials where the atoms have greater interaction with neighbors, but also from materials with less anisotropy.

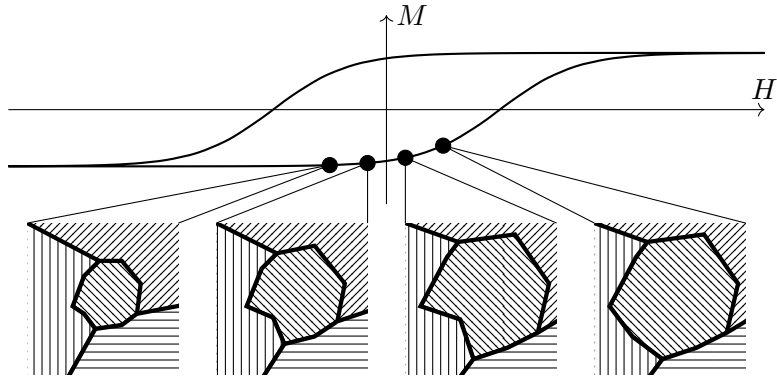
As seen, when an external field \mathbf{H} is applied, the atomic dipoles have a tendency to align. This goal can be accomplished in two ways: either all the dipoles in a misaligned domain move together or the more ill-oriented domains reduce their size. In the first case all the atoms must invest some energy to go against the local domain field, that is currently in the wrong direction. This is not energetically favored, so it does not happen.

With the shrink of the less aligned domains we witness a movement of the walls, with the atoms near the side of the more aligned domain that starts to realign.

Since the shrinking domains do not completely disappear, the magnetization field never come to a complete saturation. Instead, it assumes intermediate values that try to follow the ones of the external field. In this way we have the hysteresis phenomenon. To a value of the external field does not correspond only one value of the material magnetization field, but it depends on the past history. This also lead to some properties of the ferromagnetic materials, like the coercivity or the remanence, that make possible the construction of magnets.

1.3.4 Barkhausen noise

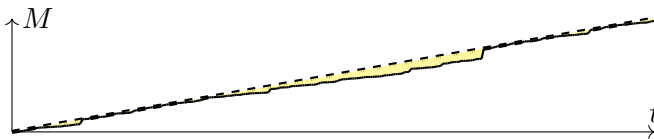
When domain walls move, they can get stuck in imperfections of the lattice, that can come from dislocations, impurities, tensions and much more. The atoms that resist to



(a) Magnetic domain growing under the effect of a slow varying external field in a hysteresis curve.



(b) Magnetic wall stuck in an imperfection which is then absorbed. The region that the domain should have occupied is highlighted .



(c) Effective magnetization (full line) versus the expected one (dashed line). The difference is highlighted.

Figure 1.10: Barkhausen noise physics. While the domain is growing, its wall encounters an imperfection where it gets stuck. The region around the imperfection should have another local field, so this is the physical area that contributes to the deviation from the ideal hysteresis curve.

align with the others slow down the wall movement, preventing the neighbors from properly aligning. This creates a deviation from the expected magnetization curve of the material, since a smaller number of atoms are aligned with the magnetization field. If the external field that caused the wall movement increases even more, the total field can be big enough to force the flip of misbehaving atoms. Now the wall can proceed its movement, even with a small acceleration due to the accumulated delay. These fluctuations in the magnetization curve are called Barkhausen jumps. They are stochastic events, since they depend on the exact realization of domain configuration that brought to the stuck wall.

Every deviation in the magnetization field variation from the expected rate imply a deviation in the ideal force that an electromagnet exercises. Therefore, the expected

position of a coil actuator can have very small imperfections, that reflects the ones of the domain wall speed.

Those magnetization deviations can also be picked up with a coil, in which small induced potentials are created. In this way the phenomenon has been measured and characterized in the past. A pickup coil has been put around a piece of ferromagnetic material in an external magnetic field and the signal has been amplified. The integral of the resulting amplified signal reflected the imperfect magnetization curve of the studied material.

1.3.5 Barkhausen noise as crackling noise

When we think about the dynamics of walls domains we discover that there can be many frequent, small imperfections of the lattice that cause many small Barkhausen jumps. Instead, big jumps will be significantly influenced only by larger, rarer imperfections. This made the Barkhausen noise a kind of phenomena that presents self-similarity, since the presence of the same mechanism at different scales.

Noisy processes with self-similarity are called crackling noise, that is a class of phenomena that comprehends things like avalanches and earthquakes [15].

Measurable quantities from this effect will also present the property of self-similarity: an example is the shape of the signal taken with the pickup coil cited in the precedent section. Those signals are composed by many small spikes and some greater ones, with a fractal-like structure. The larger spikes, scaled down, will be similar to the smaller one.

Assumed the self-similarity of an event, the mean behavior can be expressed as:

$$\langle x \rangle(t, T) = T^\mu x\left(\frac{t}{T}\right) \quad (1.10)$$

with x the variable that represent the signal, T its duration and μ some characteristic exponent.

This equation expresses that the average signal in an event will be proportional to a scale factor, that is a power of the duration itself, and a universal law, written in fraction of the signal duration.

The equation expresses the requirement of scalability of the phenomenon, so for a good model it must be possible to find a universal law. This law characterize the events that we want to model, so its shape must be coherent with the one of crackling noises.

1.3.6 Random walkers

The entity of a single deviation event can be modeled with the following equations:

$$\begin{cases} x(t=0) = 0 \\ x(t+\delta t) = x(t) + \xi(t) \\ x(t_{\text{stop}}=0) = 0 \end{cases} \quad (1.11)$$

where the deviation starts and ends at zero, and $\xi(t)$ is the increment which is a random variable. This models the deviation as a random walk excursion.

Random walks can have many kinds of increments, but the one that better adapts to the Barkhausen noise is the one used by Lévy walks [16, 17]. The distribution of their increments follows a power-law distribution, in the form:

$$f(\xi) \sim \frac{1}{|\xi|^{\alpha+1}} \quad (1.12)$$

so this kind of walks needs a parameter: the *power index* α . This parameter is bound to the interval $]0, 2]$, since values greater than that will present a converging distribution, that does not have long jump unlike the Barkhausen phenomenon we want to model.

The produced walks have a characteristic shape, with many sudden changes of direction, coming from the heavy tails of the increment distribution. With lower *power indices* larger walks appear more squared, because the walkers can make a very long jump that brings it far away from the origin, up to an equally long jump in the opposite direction. While the walker is far away, it can make many smaller jumps, just like a stuck magnetic wall can make many small adjustments before surpassing the imperfection.

The universal law for Lévy walks has been found to have the form of a semicircle [17]. An example is shown in Fig. 1.13 where are plotted means and medians of 1000 walks for different *power indices*.

The mean excursion in the interval $[-\frac{T}{2}, \frac{T}{2}]$ will then have the shape:

$$\langle x \rangle(t, T) \propto T^\mu \sqrt{1 - \left(\frac{2t}{T}\right)^2} \quad (1.13)$$

So an excursion from a Lévy walk can model a crackling noise pulse.

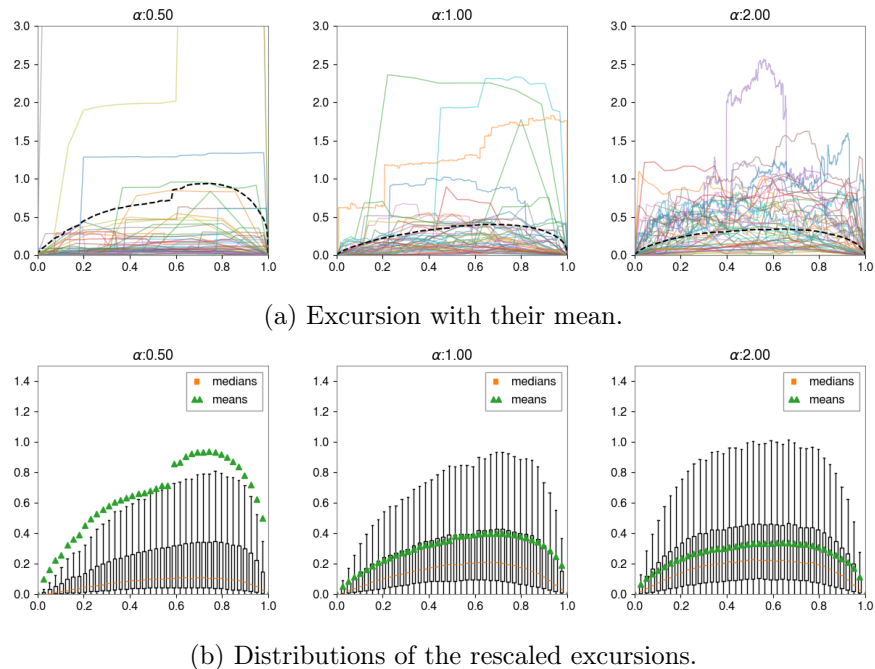


Figure 1.11: Rescaled excursions from random walkers with different power indexes.

1.4 Glitch occurrence

Glitches often appear in small groups. We can have hours of detection without them, but then, suddenly, a group of glitches, with intermissions as close as seconds appears. Because of this, the model we make for the glitches must account their occurrence in groups.

1.4.1 Bursts and intermittency

The many close events compose the bursts, and are separated by long intermissions. Those burst represent a turbulent phase of the system, as it follows a chaotic dynamics, with irregular groups of events of variable lengths. In our model of glitch, we can picture these bursts as moments when the Barkhausen noise has a greater activity: it can be for some internal reasons, like a regime of the ferromagnetic material where there are more intense Barkhausen jumps, but also it can come from a moment when is needed greater adjustment by the actuators, so there is more external field applied.

The result is an intermittent behavior that, for some period of time, "turns off" the noise. These long intermissions also do not have a regular duration: there is some randomness in the way they are generated.

The intermittent behavior of the system is a feature I want to reproduce, with a model capable of generating the times to associate to the single events.

1.4.2 Dissipative dynamical systems

A kind of system that shows the aforementioned properties is the discrete dynamical system described by the equation [18]:

$$x_{n+1} = f(x_n) = ((1+b)x_n + (1-b)x_n^z) \mod 1 \quad (1.14)$$

where b and z are the two parameter of this model, and are respectively called *expansion coefficient* and *universality class*.

If we study the graph of the function of this system we can easily find the two kind of regimes we wanted to reproduce:

- a **laminar phase** when the variable is well below values that go against the modulus cut, in Fig. 1.12 is represented as the red area of the graph;
- a **turbulent phase** when the modulus operator forces the variable to return to smaller values, in Fig. 1.12 is represented as the blue area of the graph.

The laminar phase is characterized by a slow raising of the variable, slower with smaller second term of the equation. We can find a value \tilde{x} that represents the end of this phase as the point where the function presents its (first) discontinuity.

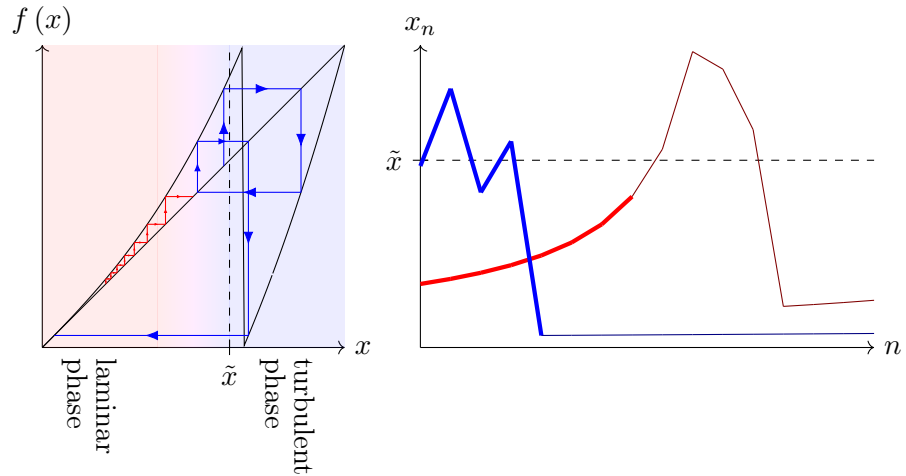


Figure 1.12: Laminar and turbulent phases for the system. We can see how the red trajectory, in the laminar phase, presents a monotonic increase. The blue trajectory that crosses the turbulent zone is pushed back below \tilde{x} , but only for a short period of time.

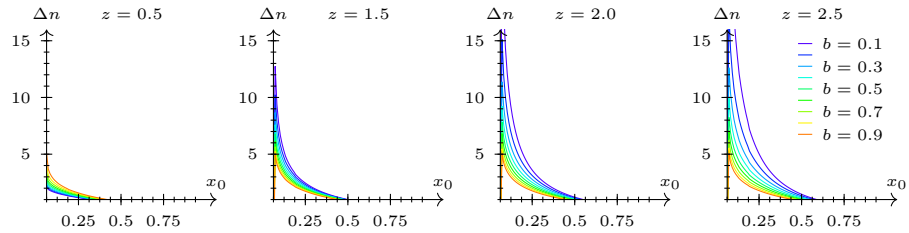


Figure 1.13: Intermission lengths Δn in function of the starting point x_0 , for some values of the burst model parameters.

We can see that this laminar phase is completely predictable, knowing only its initial value. The duration can be found integrating the equation

$$\frac{dx_n}{dn} \simeq x_{n+1} - x_n = bx_n + (1 - b)x_n^z$$

that is the continuous limit of the discrete dynamical system, for $x < \tilde{x}$. If we set the upper limit of the x_n integral to one, we find that the duration Δn is:

$$\Delta n = \frac{\ln(b(x_0^{1-z} - 1) + 1)}{b(z - 1)} \xrightarrow{x_0 \rightarrow 1} \frac{x_0^{1-z} - 1}{z - 1} \quad (1.15)$$

with a power-law trend for big values of the starting value, or small intermission times. A plot of the intermission times for some values of the parameters is in Fig. 1.13. This suggests that if we have a uniform probability of starting from a random point in the interval $[0, \tilde{x}]$, the lengths of the laminar phase will initially follow a power law distribution. For small values of x the waiting times stop to follow the power law, so they become larger and larger. This creates a knee in the distribution of waiting times, so larger intermissions will be less likely. This makes the probability of having to wait very long times for a glitch to happen very low.

When the laminar phase ends, the variable with value greater than \tilde{x} will be brought back to a smaller value. This creates a spike in the series of values. As seen before, there is a great probability to have a short ascent, so the next spike will be generated shortly after the last one. This continues, until a return to small values, where the laminar phase begins again.

Equivalently to the study of the spikes in a series of values from a realization of this system, we can study the signal obtained injecting a specific shape every time the values from the set intersect a threshold. In this way, the injected shapes will have the same distribution of times of the spikes.

Therefore, if we want a way to simulate the signal from a Barkhausen noise source, we can inject in a background an excursion from a Lévy walk every time a dissipative dynamical system spikes.

CHAPTER 1. INTRODUCTION

Know your glitches

In this chapter I will discuss how I generated glitches from the detector given noise ASD and the random walk model. I will then explain how I studied these glitches, analyzing their shapes and extracting some quantities, that can be useful to understand the model used to generate them.

2.1 Method

The first thing to do when we have a new model is to check if it can reproduce the phenomenon that is trying to describe.

In this case, since the observed phenomenon is non-deterministic, we can only start from checking if a set of products of the model appears similar to the observed sets of glitches.

2.1.1 Glitch generation

As discussed in §1.3.6 the disturbances introduced by the domain walls irregular motion in a ferromagnetic system can be modeled as Lévy random walk. So, the abnormal signals from the detector therefore can be created injecting an excursion in a realization of the detector Gaussian background noise.

The excursion can be simulated by generating steps increments (ξ_n from the equation 1.11) as random values drawn with the chosen distribution.

The distributions I chose to use are:

$$f_{Gauss}(x_{n+1}; x_n) \sim e^{-\frac{(x_n - x_{n+1})^2}{2}} \quad (2.1a)$$

$$f_{Cauchy}(x_{n+1}; x_n) \sim \frac{1}{1 + (x_n - x_{n+1})^2} \quad (2.1b)$$

$$f_{Lévy}(x_{n+1}; x_n, \alpha) \sim \frac{1}{|x_n - x_{n+1}|^{\alpha+1}} \quad (2.1c)$$

where x_n and x_{n+1} are the position of the walker before and after the step.

The Gaussian and Cauchy distributions are initially chosen to be a test for the walk generator. For the power-law walks, I generated four sets, one for each of the following power index α : 0.5, 1.0, 1.5, 2.0. This is the first parameter of the model.

Since we are only interested in a single excursion all walks start from zero. The steps are done one by one, checking every time for a zero crossing. The last value, the one with different sign, is then replaced with a zero.

Proceeding with this way of generating excursions, the length of one of them can vary, following the natural distribution of this kind of process. A maximum length of 5000 iteration is set to generate only glitches with duration under one second. Every walk that goes over this limit is discarded and regenerated.

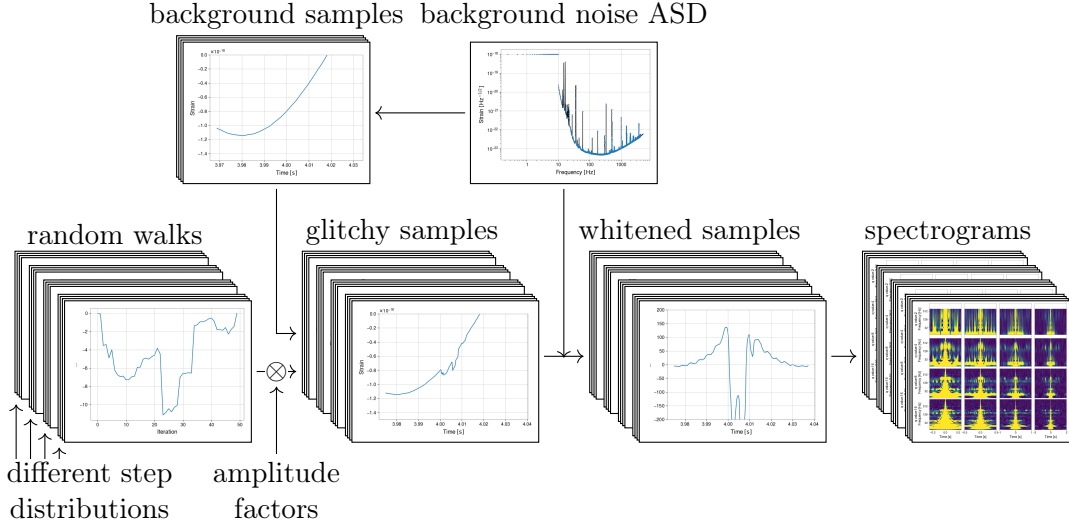


Figure 2.1: Workflow of the glitch generation. Some background noise samples are created from the ASD of the detector. Every sample is combined with random walks from different step distributions obtaining glitchy samples, that are whitened with the original ASD. The whitened samples can be displayed as spectrograms, or used for further analysis.

For every step distribution I created a file containing ten hundred generated walks.

Now that the excursions are created, I worked on the simulation of the backgrounds samples where the walks will be injected. Those samples are generated with the following this procedure:

Estimation of the noise spectral density The number of sample points n to be generated is chosen to give a sample with a duration of eight seconds, so that it is long enough to contain all the possible time widows that can be used in the analysis. The amplitude spectral density of the detector is then interpolated with a monotone cubic interpolator. It has been chosen for its property of avoid overshooting, useful with an ASD that have many lines.

Noise spectra For every interpolated frequency except the first and the last, two random numbers with normal distribution are drawn. For the zero and the Nyquist frequency only the real component is computed, as a real signal will not have imaginary components for these frequencies. All the drawn complex numbers are multiplied by the interpolated frequency, obtaining a random noise spectrum with the same average shape of the detector noise ASD.

Samples generation and storing Every generated noise spectrum undergoes an inverse Fourier transformation to obtain the desired Gaussian noise sample. The

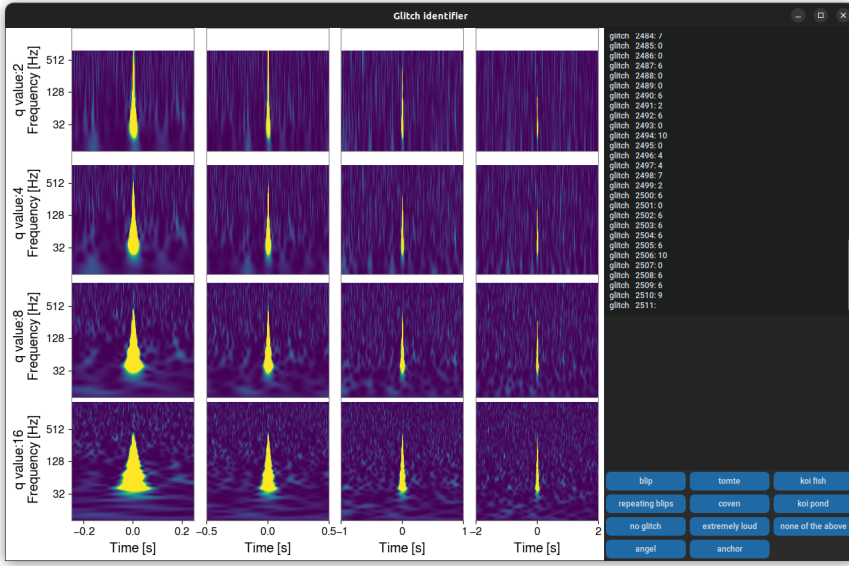


Figure 2.2: Interface of the program used to manually identify the glitches. The displayed glitch is a case where with different q-values the shape of the glitch varies sufficiently to leave its classification uncertain between a *tomte* and a *blip*.

corresponding times for each point are computed. The times and all the background samples are stored in a file.

The only thing left to do is to inject the walks into the background samples, to obtain the glitchy samples.

The walks are multiplied by an amplitude factor a before injecting them in the backgrounds. The amplitude factors are drawn from a uniform distribution in logarithmic space in the range $10^{-24} \div 10^{-18}$. This amplitude factor is the second parameter of the model, while the first was the power index α

The obtained glitchy samples are whitened with the previously interpolated amplitude spectral density.

2.1.2 Glitch identification

Then, I proceeded comparing the generated glitches with the real ones. I have done it by using the same visualization used in the Gravity Spy project[12].

From every whitened sample I obtained a plot with many spectrograms using the q-transform from the GWpy package[19]. Each subplot has a different combination of q value and time window size. The q values are in the range $2 \div 16$ while the window sizes varies between $0.5 \div 4$ s, like the one used by Gravity Spy.

Following some other of their choices, the color map has a cutoff for the normalized

CHAPTER 2. KNOW YOUR GLITCHES

energy at 25, so over this value it saturates with a yellow.

The set of q-plots for a glitch is then rendered, waiting for a user identification with a self-made script (see Fig. 2.2 for the interface). I cataloged 2400 glitches for every step distribution mentioned in §2.1.1 in one of the following categories, inspired by the ones of Gravity Spy:

- **blip** glitches that are symmetric, short in time and have tear-like appearance;
- **tomte** glitches similar to the blips, but are lower in frequency and have a truncated base;
- **koi fish** loud blips with a symmetric structure at low frequencies that resembles the fins of this kind of fish;
- **repeating blip** more than one blip generated in one glitch;
- **coven** more than one tomte generated in one glitch;
- **koi pond** more than one koi fish generated in one glitch;
- **no glitch** signals where the glitch is not distinguishable from the background;
- **extremely loud** glitches that saturate almost all of the q-plot;
- **none of the above** glitches that does not resemble any other one or do not have a recognizable shape;
- **angel** loud blips with symmetric features at high frequencies;
- **anchor** loud glitches with both the low and high frequencies features from koi fish and angels.

A glitch is considered to be in a category with repeating figures (like *repeating blip*, *coven* or *koi pond*) if the single base shape is still recognizable. I added to the known categories these last two as sometimes I found some of these glitches. Also the *angel* and the *anchor* categories do not belong to the original ones. I wanted to add these to differentiate the glitches with the high frequency feature from the others, but they can be considered sub-categories of *blips* and *koi fish*.

Quiet glitches with a regular round shape and that do not display any peculiar feature are categorized as blips.

Once a glitch is identified its amplitude factor and type are saved in a file. So, for other analysis, this information can be combined via a unique identifier to the corresponding samples.

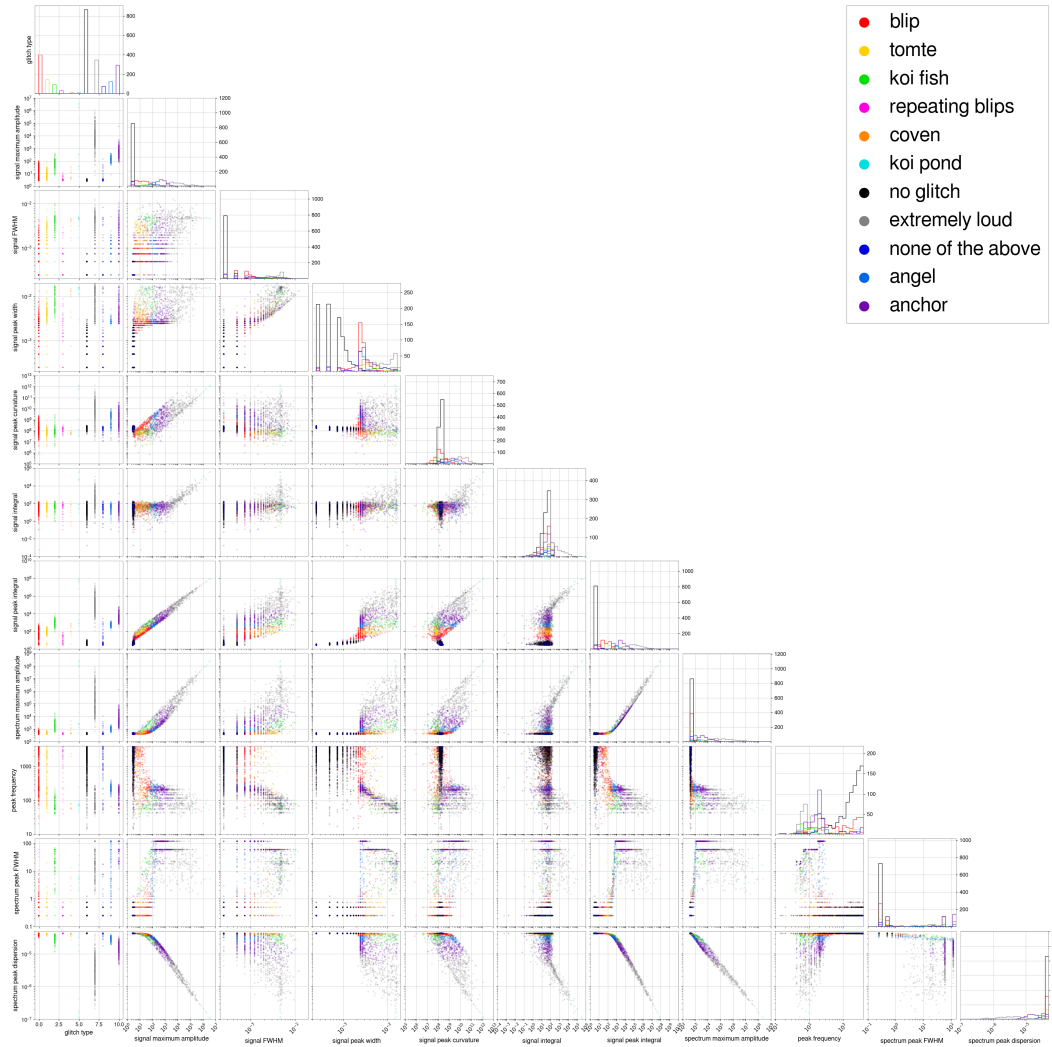


Figure 2.3: Portion of the corner plot for the quantities computed for the glitches. Each glitch type is represented with a different color.

2.1.3 Glitch analysis

To better understand the characteristics of these generated glitches, like which feature every glitch category has, I proceeded with the analysis of the signals.

All the identified glitches are loaded and analyzed. I defined a set of quantities, some of them are computed from the walk, some of them from the whitened signal and some of them from the spectrum of the whitened signal.

A couple of quantities come from a fit done over the walk: as stated in §1.3.5 the excursions can be compared with a semicircle. The diameter is set to a fixed size as big as the length of the walk, and a scale factor for the vertical axis become the parameter of a fit.

The complete list of computed quantities is:

- **walk length** obtained by counting the number of points of the generated walk, including the first and the last zero points;
- **walk amplitude** the maximum amplitude of the walk, as the maximum distance from the zero axis during the excursion;
- **walk maximum step** the longest step done by the walker;
- **semicircle amplitude** the vertical scale factor of the fitted semicircle;
- **semicircle χ^2** mean deviation from the semicircle law;
- **sign** the sign of the first non-zero value of the excursion;
- **signal maximum amplitude** the maximum value of the whitened sample module;
- **signal FWHM** the distance between the nearest intersections of the whitened signal with half of the maximum amplitude;
- **signal peak width** the distance between the closest zero-crossings around the signal peak;
- **signal peak curvature** the second derivative estimated at the peak of the whitened signal;
- **signal integral** integral of all of the whitened signal;
- **signal peak integral** integral of the whitened signal between the two closest zero-crossings around the peak;
- **spectrum maximum amplitude** the maximum of the spectral density module;
- **peak frequency** the frequency of the peak of the spectrum;
- **spectrum peak FWHM** the distance between the nearest intersections of the spectral density of the whitened signal with the half of the peak height;

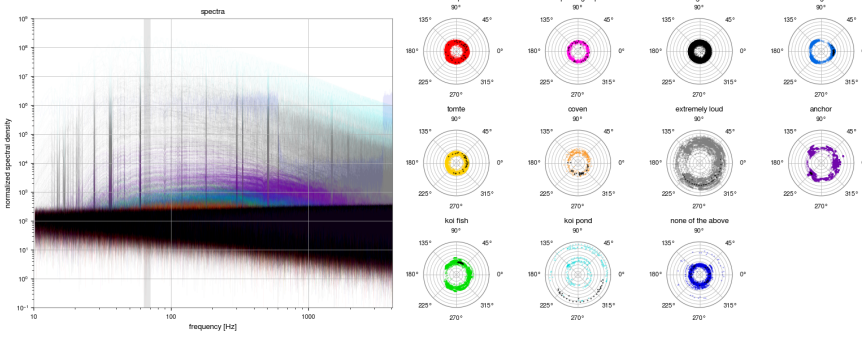


Figure 2.4: Portion of the complex spectra for different glitches subdivided by kind. We can see some differences between different categories, as for some of them we have a grouping for the phases.

- **spectrum peak dispersion** the momentum of inertia of the spectral density of the whitened signal computed in log space.

All the quantities are then stored in files. The data is also rendered in a corner plot, coloring the points by their associated glitch type, as shown in Fig. 2.3.

The glitch categories are also analyzed by overlaying all the whitened samples of the same category, searching for similarities. The same plot is done with the spectral density of the signals, and some common features can be observed.

The observations led to further analysis of the spectra, evaluating also the complex nature of this quantity. Since the frequencies span many orders of magnitude, I choose to analyze a small portion of the frequency interval at a time. So, the frequency span in the logarithmic space is subdivided in many intervals, with the size of one tenth of an order of magnitude. Then, for all the glitches of the same type, portion of the spectra is plotted onto the complex plane as in Fig. 2.4. Comparing the graphs of different kind of glitches gives us information about the characteristics of every category.

One last analysis regarding the glitch types is the one done by searching common features in the q-plots of all the glitches of the same category.

Since the plots saturate, one of the things that cannot be directly seen is how big the maximum value is. The presence of high values make the mean and other kinds of statistics diverge, leading me to use the quantiles.

The quantiles can be computed for every pixel of the image, giving an idea of a common shape of the glitches for every category. Varying the portion considered by the computed quantile, we can see different features of the glitches. An example is in Fig. 2.5.

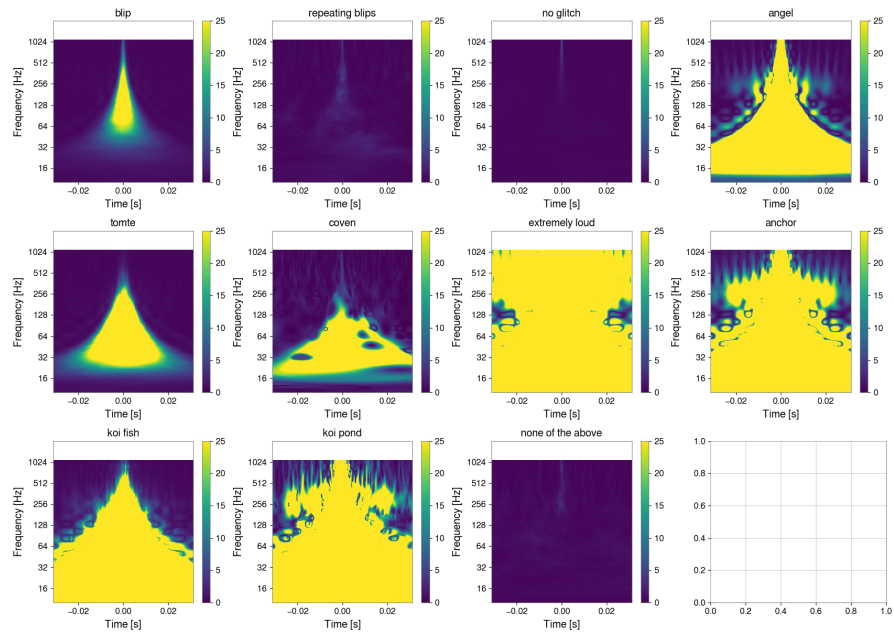


Figure 2.5: Median pixel by pixel of all the computed q-plots of the simulated glitches in the same category.

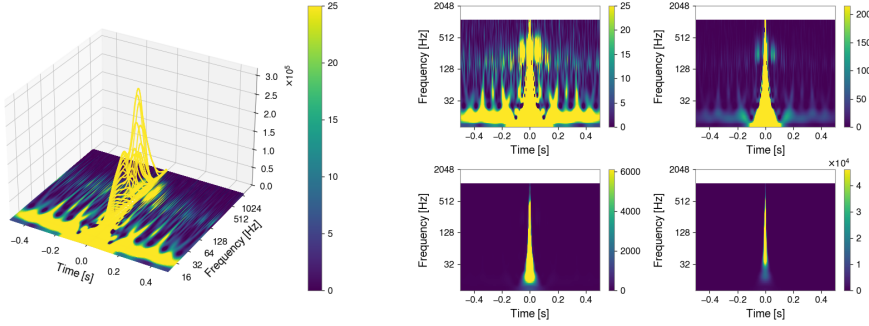


Figure 2.6: The spectrogram displayed with a non-standard representation. At the left, a tridimensional graph of the q-transform, with the usual color range. The plots on the right cover different ranges of values, showing how much the glitch shape depends on this quantity.

2.2 Observations

During the identification process, as well as during the analysis of the signals, I found some recurring patterns. In this section I will be discussing some of the observations I made and discuss the possible causes of these phenomena.

2.2.1 Glitch morphology

The whitening process can greatly affect the shape of a signal. I have observed that, comparing a signal before and after the whitening, many times it will be broadened, with dips appearing around the injected walk. Sometimes these induced fluctuations will grow so much that their amplitude becomes greater than the injected walk itself, that can be filtered out.

The shape of the ASD used in the process is fundamental: peaks of noise result in frequencies that are mostly silenced. So, the ASD of whitened signals shows some lines that resemble the one of an absorption spectrum. Part of detector ASD with lower noise, on the other hand, adds some power to the signal when the whitening process takes place. I observed that glitches with a greater amplitude are more likely to show some lines at higher frequencies, due to a minimum in the detector ASD and the fixed range of the spectrogram.

Also, the q-value of the q-transform used to render the glitches can be important for their morphology. A large group of *blips*, the ones that have a lower frequency near one of the whitening absorption lines, can be truncated resembling a *tomte*.

If a lower q is used, the transformation used spreads the information better along frequencies. The most affected part is the one at lower frequencies, where many glitches assume a rounder shape. Higher q smooths the times more, broadening the bases of the

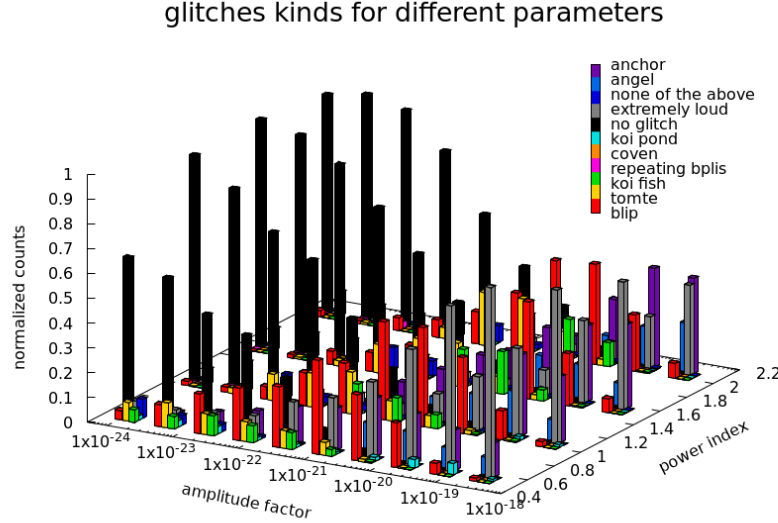


Figure 2.7: Glitches populations obtained with different parameters of the model. We can see how this is the only useful region of the parameter space, as at the limit all the glitches become part of the *no glitch* or the *extremely loud* categories.

glitches and localizing the absorption effect. Also, the tail can be diluted in more tiles, vanishing. This mechanism brings a greater confusion for *blips* and *tomtes*, giving more uncertainty to the distinction of these categories.

The morphology seems to depend on the walk steps distribution.

Gaussian walks and power law with higher power index can produce *tomtes* that better resembles the real ones. The cause can be found in the lighter tails of the distributions, that suppress longer steps and give a smoother walk. A long step generates discontinuity, that implies a greater contribution at higher frequencies.

Distributions with lower power index are more likely to produce glitches of one of the multiple categories. This phenomenon is caused by the greater probability of a long jump in an outward direction. This brings it to a longer walk, with the chance of many long jumps that creates multiple bursts of energy at high frequencies. All those bursts are whitened in glitches, so the probability of creating a group increases.

Due to a larger mean walk amplitude, glitches with the same amplitude factor have a greater likelihood to become louder if the step distribution has heavier tails. These kinds of walk are more inclined to saturate the spectrogram, reducing the range of realistic amplitude factors.

All these factors contributes to have different ratio of glitch population with different parameter of the model as shown in Fig. 2.7.

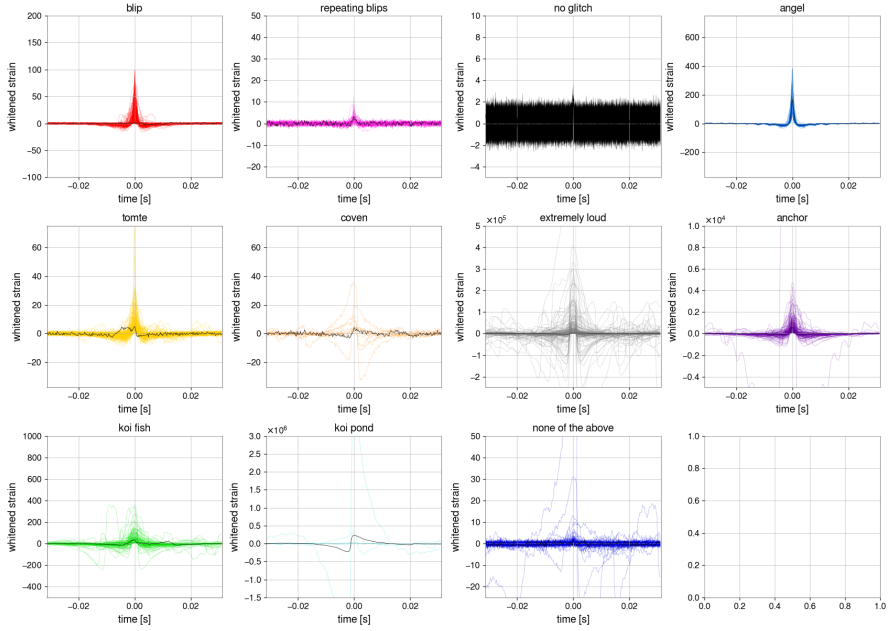


Figure 2.8: Whitened signals of the catalogued glitches. All the glitches have been aligned by the time of the peak. Every plot has a different amplitude range, the more appropriate for every category, while the scale of times is always the same.

2.2.2 Glitches in other spaces

Another obvious way to study the produced glitches is by observing the whitened signal they produce. To study the more general behavior, I decided to overlay the whitened strains for every catalogued glitch. This brought me to the observation of some common characteristics among the groups.

We can see from Fig.2.8 how only a very specific kind of signal became an *angel* glitch. Only short and loud signals can produce this kind of spike. Then *angels* glitch are a louder type of some *blips*, where the greater amplification excites the emission line in the fixed range spectrograms.

We can also appreciate how the *tomtes* are a type of glitch that comes from longer walks, when compared with the *blips*. This can be deduced by the broader peak that they present. The *koi fish* are glitches where the length of the walk and the amplitude factor combines, creating a glitch that has large, multiple and closer oscillations.

The effects of the whitening process can be appreciated even more on the glitch spectrum. In all the louder categories, where Gaussian noise is smaller, all the previously described absorption lines are really pronounced. The shape of the ASD is also clearly the reciprocal of the amplitude spectral density used for the whitening. Thus, the shape of the glitch ASD mostly came from this process.

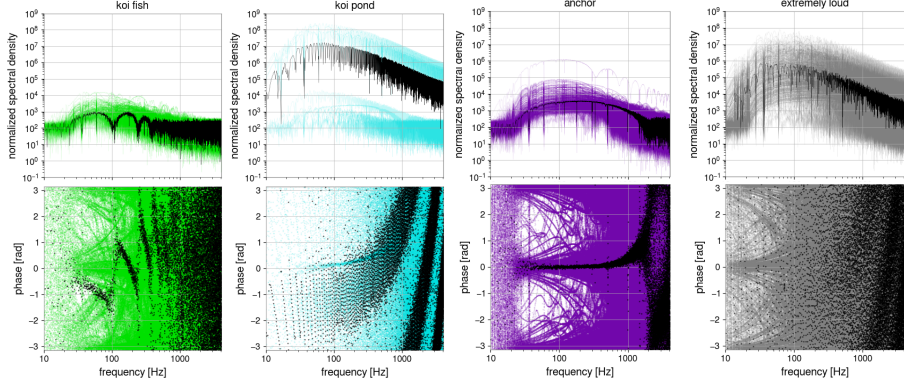


Figure 2.9: In this plot we can appreciate the oscillating nature of the spectrum of the *koi* categories compared to the *anchor* that have less oscillations and the extremely loud that have an even more complicated phase.

Once plotted the glitch spectra as in Fig. 2.9 I observed that all the ones that come from the *koi* categories present some oscillations. This induced me to also inspect the phase of these complex numbers.

When we plot the phases against the frequencies, we see that the graphs have bumps at the same frequencies of the amplitude oscillations. A possible cause is the walk shape, which can have many sharp corners. Those that can produce a portion of the strain with a more rectangular shape, so the corresponding Fourier transform will resemble the sinc function.

At very high frequencies, above the kilohertz, the spectrum of almost all the glitches returns to be dominated by the random Gaussian noise, ceasing to have useful information. The phase also returns to have a uniform distribution.

2.2.3 Glitch quantities

As described in §2.1.3, some quantities have been computed for every glitch. These quantities can be used to discriminate some categories of glitches but also can help us by giving more information about the glitches that can be produced.

One of the most interesting graphs obtained is the one that shows where the different populations of glitches are located in the plane created by the quantities *amplitude factor* and *walk length*, shown in figure 2.10. It can be seen how well the glitches groups, indicating that these two quantities are fundamental for the glitch morphology.

This plot confirms that some louder glitches, like *koi fish*, *anchors* and *angels* are only *tomtes* and *blips* with a greater amplification.

There is another interesting property regarding most of the computed quantities. For all

2.2. OBSERVATIONS

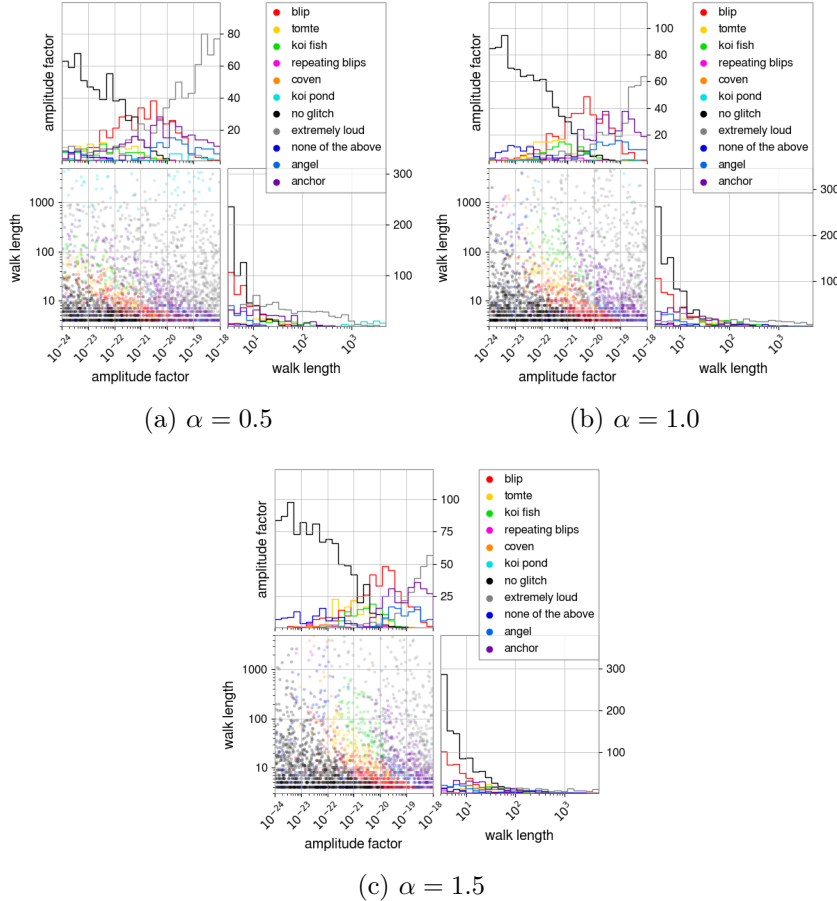


Figure 2.10: Amplitude factors and length of cataloged glitches. We can see how every category stays in a different portion of this space. We can also see how the distribution changes with different power indices.

the glitch categories that have some defining features (unlike *no glitch*, *extremely loud* and *none of the above*), the distribution seems to have a fixed range. This can be good news when we think about the definition of every category, because this indicates that the definitions are well-formed. By the use of some quantities we can try to discriminate between the useful categories (like *blips* and *tomtes*, for which we know the statistics) and the useless ones (the three without features) for which a real dataset is partial or can be contaminated by other phenomena.

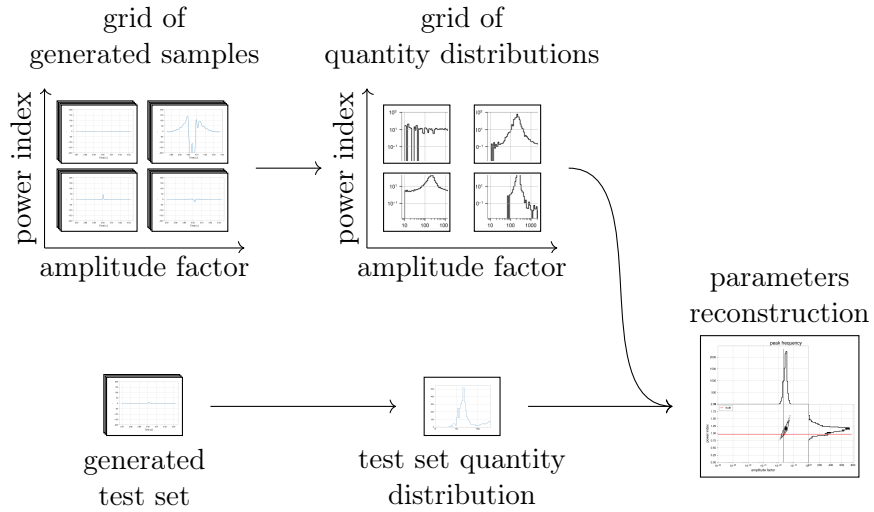


Figure 2.11: Workflow of the test of the fit procedure. A large number of samples for every point of a grid in the random walk parameter space are generated. Their quantities are computed and the distributions estimated. A test set is generated and its quantity distribution compared with the one of the grid to reconstruct the generation parameters.

2.3 Finding the parameters

Once the products of the model have been studied, and verified that they resemble the real phenomena, it is time to characterize the model itself.

In this case the model has two parameters, so I am going to build a procedure that can reconstruct their value from a given set.

2.3.1 Likelihood of a quantity

The quantities described in §2.1.3 also find an application in the estimation of the parameters of the random walk glitch model. The two parameters we are interested in are the *amplitude factor* a and the *power law index* α , both used to generate glitches.

The distribution of one of the quantities can be estimated for a fixed parameter set $\Theta = (a \ \alpha)$ by a Monte Carlo simulation. I have made it by generating a large number of glitches ($N=500.000$) and computing the desired quantity for every glitch. From the set of computed quantities I obtained the corresponding histogram, subdividing the entire range in $N_{bin} = 50$ bins.

From now on the counts of quantities contained by each bin of the histogram are indicated as $n_i(\Theta)$. The estimated probability of measuring a quantity in the interval covered by the i th bin is then

$$\tilde{p}_i(\Theta) = \frac{n_i(\Theta)}{N} \quad (2.2)$$

with a count uncertainty of $\tilde{\sigma}_{ni}(\Theta) = \sqrt{N\tilde{p}_i(\Theta)(1-\tilde{p}_i(\Theta))}$.

With my construction of the histograms, in the case of a uniform distribution the relative uncertainty of the estimated probability converges to

$$\frac{\tilde{\sigma}_{pi}}{\tilde{p}_i} = \frac{\tilde{\sigma}_{ni}}{n_i} \simeq \frac{\sqrt{N\tilde{p}_i}}{n_i} = \frac{1}{\sqrt{n_i}} = \sqrt{\frac{N_{bin}}{N}} = 1\%$$

With a theory that has the parameters Θ_{th} to which follows the probability $p_i(\Theta_{th})$ for each i bin. The likelihood of obtaining a histogram with counts \mathbf{m}_i from a set of M glitches is then the multinomial likelihood $\mathcal{L}(\mathbf{m}_i; \Theta_{th}) = M! \prod_i^M \frac{p_i(\Theta_{th})^{m_i}}{m_i!}$. We can compute the logarithm of this likelihood using estimated probabilities, obtaining the expression:

$$\ln \mathcal{L}(\mathbf{m}_i; \Theta_{th}) \simeq \ln(M!) + \sum_i^M m_i \ln(\tilde{p}_i(\Theta_{th})) - \sum_i^M \ln(m_i!)$$

Utilizing the eq 2.2 for the estimated probabilities we obtain:

$$\ln \mathcal{L}(\mathbf{m}_i; \Theta_{th}) \simeq \ln(M!) + \sum_i^M m_i \ln(n_i(\Theta_{th})) - \sum_i^M m_i \ln(N) - \sum_i^M \ln(m_i!)$$

Where only the second term varies with the parameters of the theory, so we can group all the other terms in an expression $k(\mathbf{m}_i)$ that is a constant for a fixed dataset.

$$\ln \mathcal{L}(\mathbf{m}_i; \Theta_{th}) \simeq k(\mathbf{m}_i) + \sum_i^M m_i \ln(n_i(\Theta_{th})) \quad (2.3)$$

This likelihood can be used in a Markov chain Monte Carlo to obtain the posterior distributions of the parameters. Since the first term is constant, its computation can be avoided to speed up the process.

2.3.2 Glitches discrimination

Not all the generated glitches can be used to populate the histograms. As stated in §2.2 only some of the categories of glitches can be considered useful for an analysis. The categories without features (*no glitch*, *extremely loud* and *none of the above*) can be contaminated with other kind of glitches in a real dataset. So, all the glitches in these categories must be excluded. This is accomplished by finding a quantity that can discriminate glitches of these categories from the others. The most useful quantity in this sense is the *signal peak integral*.

As shown in Fig. 2.12 the loudest and the quietest category can be mostly excluded by selecting only the glitches with quantities in the interval $10^1 \div 1.5 \times 10^4$, values that minimize the chances of misidentification. We can also see how the same interval is optimal for different values of the parameters, so its use will not affect the results.

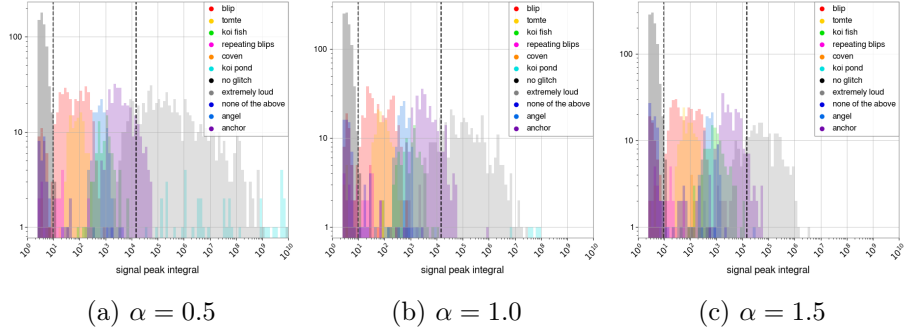


Figure 2.12: Histograms of the quantity selected for the glitch discrimination. It can be seen how well the *no glitch* category can be separated from the others, while the *extremely loud* glitches overlap with the *anchors*.

2.3.3 Computing the likelihood

We have seen what is the likelihood of obtaining a quantity histogram, and how its theoretical shape can be estimated for an arbitrary parameter set Θ_{th} with a Monte Carlo simulation. But if we want to perform a Markov Chain Monte Carlo with the likelihood, for every point of the chain we need a Monte Carlo for the histogram, making the process really computationally heavy.

I tried to calculate histograms for some points of the parameter space, with a low number of generated glitches. I noticed a certain regularity in how they vary from one point of the parameter space to another. So, I decided to obtain the estimations of the probability distribution by interpolating the histograms computed in a grid of possible parameters. The grid covers the same region of parameter space used in §2.1.1, with ten different values for every order of magnitude of the parameter a and ten different values for every unit of the parameter α .

Once generated, all the quantities that can be measured from the signals are saved with the corresponding parameters. A subsampling of the obtained histogram grid for one of the quantities is shown in Fig. 2.14.

The computation of the likelihood in a point of the parameter space is now much faster, as it only requires an interpolation of the histogram bins. A quintic spline interpolator is used for its fast evaluation, as the coefficients are computed only in the initialization phase, while retaining good interpolations.

2.3.4 Estimation tests

The process of parameter estimation is simulated by generating a small dataset of glitches with a size that is in the same order of magnitude of a realistic glitch set ($M \sim 1000$). The parameters used for the glitch generation are fixed to the arbitrary

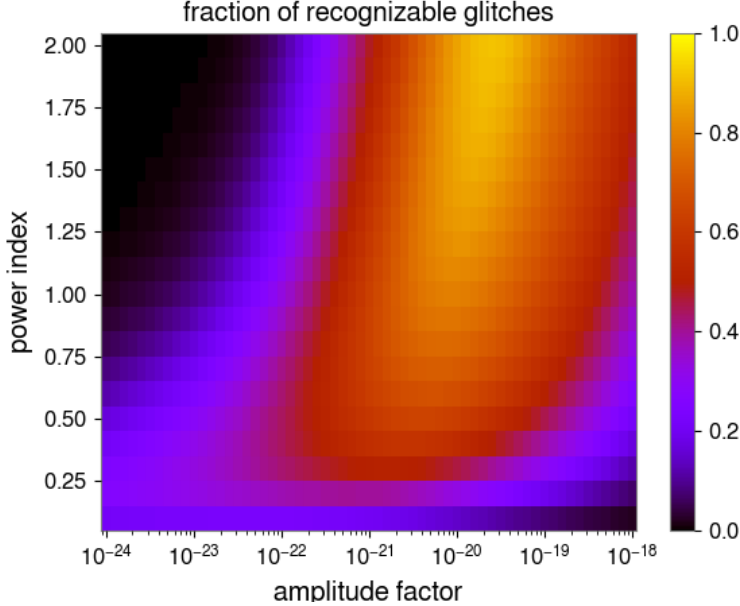


Figure 2.13: Estimated probability of keeping a glitch in function of the random walk parameters.

values of $\Theta_{gen} = (2.3 \times 10^{-20} \quad 0.97)$, chosen randomly. All the quantities that can be measured from the signals and their ASDs are computed.

The quantities set, both the ones of the simulated dataset and the ones of the grid in parameter spaces, are discriminated as described in §2.3.2. The histograms of the discriminated datasets are computed and saved separately.

As a check, the likelihoods for all the grid points and all the quantities are evaluated and plotted. From only these plots we can exclude the use of the *signal integral* quantity as the likelihood is almost flat in all the parameter space, as shown in Fig. 2.15a.

Excluding this quantity, all the others are used for a combined likelihood, obtained as a product of all the single quantities likelihoods. The resulting likelihood presents a more pronounced peak. This result seems encouraging, since it can mean a less scattered posterior distribution.

The parameters posterior distributions are estimated with a Markov chain Monte Carlo. The prior that is used is a non-informative prior that only delimit the known region of the parameter space. The emcee library is used with a burn-in stage of 500 iterations, much longer than the estimated autocorrelation time that spans in the range of 8 ÷ 80 iterations. The generated chains have a length of 10.000 points[20].

The corner plots of the chains in Fig. 2.15b show that the reconstructed distributions touch the true values of the parameters, and display behaviors similar to the ones of the

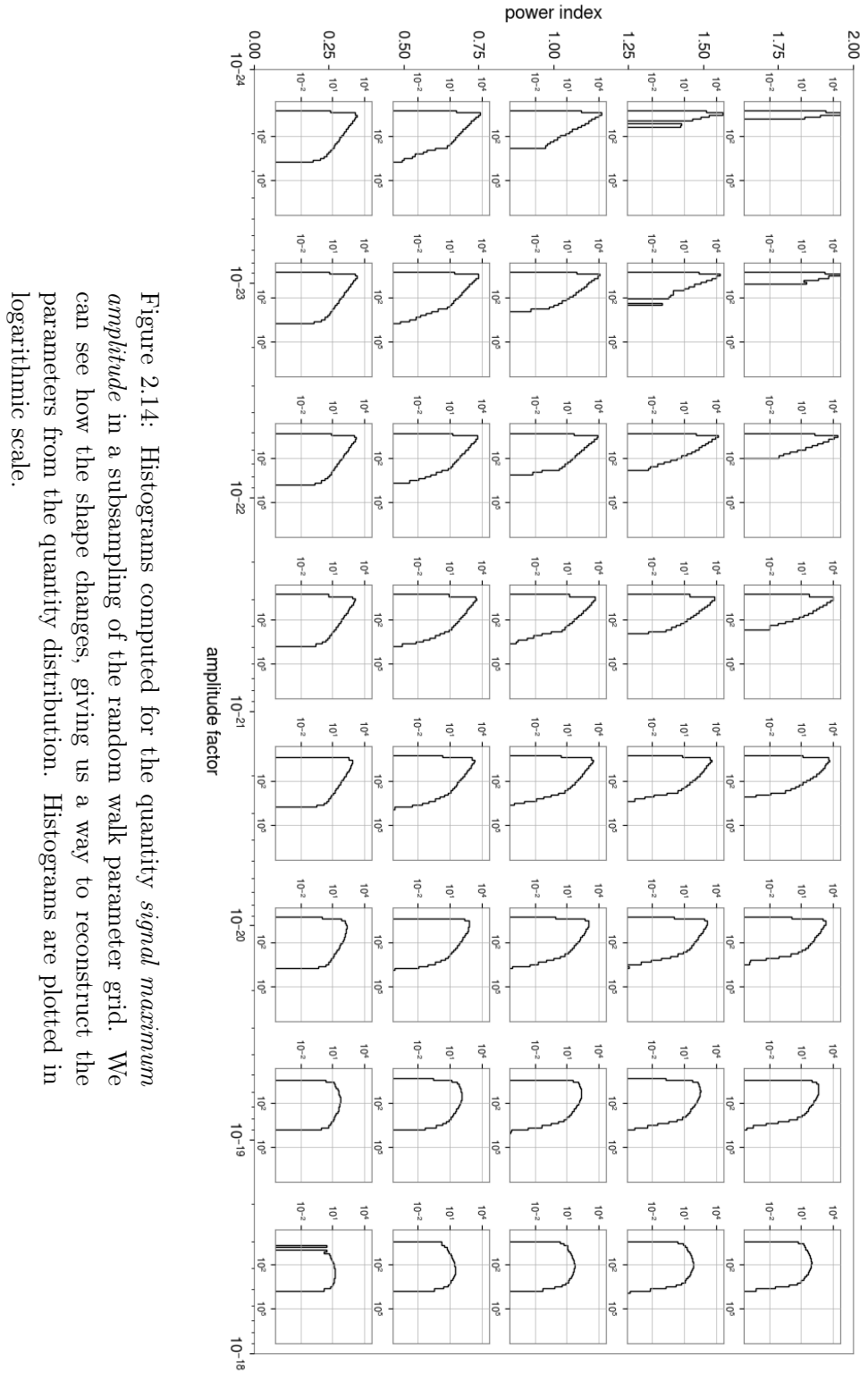


Figure 2.14: Histograms computed for the quantity *signal maximum amplitude* in a subsampling of the random walk parameter grid. We can see how the shape changes, giving us a way to reconstruct the parameters from the quantity distribution. Histograms are plotted in logarithmic scale.

2.3. FINDING THE PARAMETERS

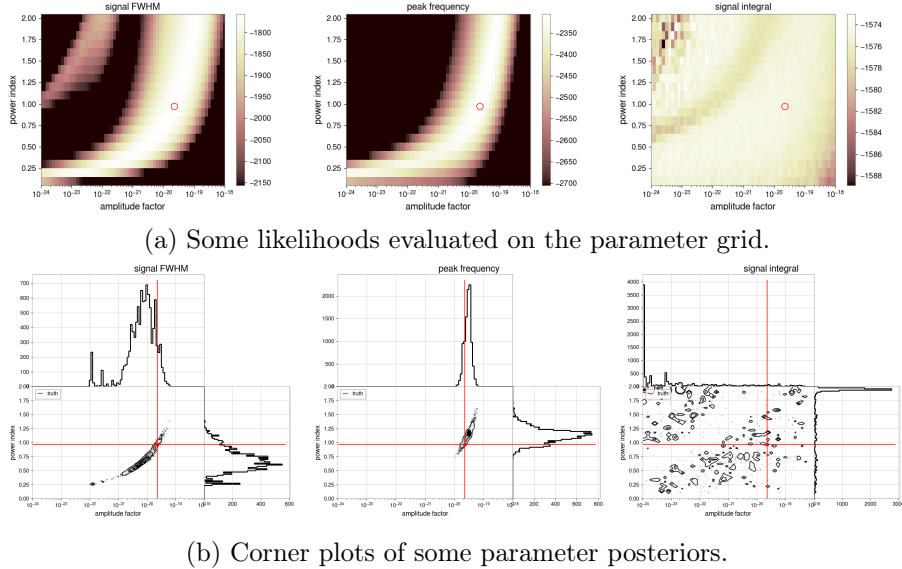


Figure 2.15: Examples of estimations with some quantities, done from a simulated dataset. We can see how the quantity *signal integral* does not give any useful information for the parameter estimation. The red point represents the true value of the parameters for the generated dataset.

likelihoods. Only few distributions are centered at the true values. It seems that all the distributions are shifted in the same way, so it can either be a bias of the estimator, or a problem of the small set realization, that has a statistic that has not converged yet. As hoped, the *combined likelihood* method show a narrower distribution.

The next step to test the estimation process is accomplished by performing estimations with different simulated dataset, all generated from the same arbitrary parameters. In this way we can study the accuracy of the estimations. By studying all the different quantities distributions plotted in Fig. 2.16 we can see how they are all scattered around the true values, so the estimation process seems to be unbiased.

We can also see how many generated cumulative distributions have a step at some lower values of the *power index* parameter. This can be caused by local oscillations in the region due to an overfitting problem of the interpolator, but it seems to not affect the shape of the distributions that much in the other parts of the parameter space.

The search for a value as a result for the estimations became a difficult task, as the position of the maximum of the likelihood seems to be greatly influenced by the defects of the interpolation method. Narrow maximum caused by already discussed overfitting problems can be very high in value, leading the optimizer to recognize the position of these peaks as a possible solution for the fit.

CHAPTER 2. KNOW YOUR GLITCHES

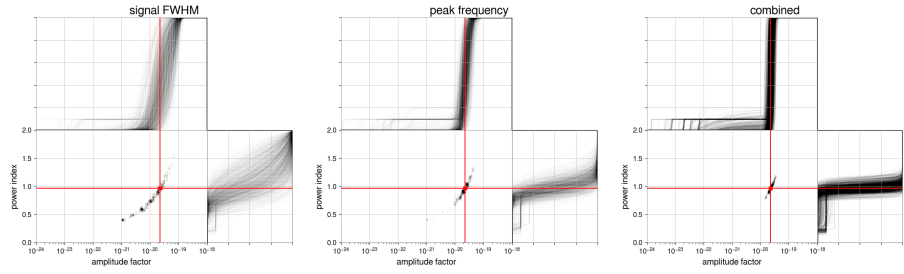


Figure 2.16: Plot of estimation simulations from different datasets, all with the same true parameters values. The first two plots show the reconstructed distribution obtained using only one quantity at a time, while the last uses the combination of likelihood.

To overcome this problem, I tried to inspect some other characteristics of the distributions of the generated chains, as means and medians. Their positions seem to be less affected by the presence of local maxima. Thus, these last two estimators are preferred to obtain a single value for the parameters.

Some examples are shown in Fig. 2.17

2.3. FINDING THE PARAMETERS

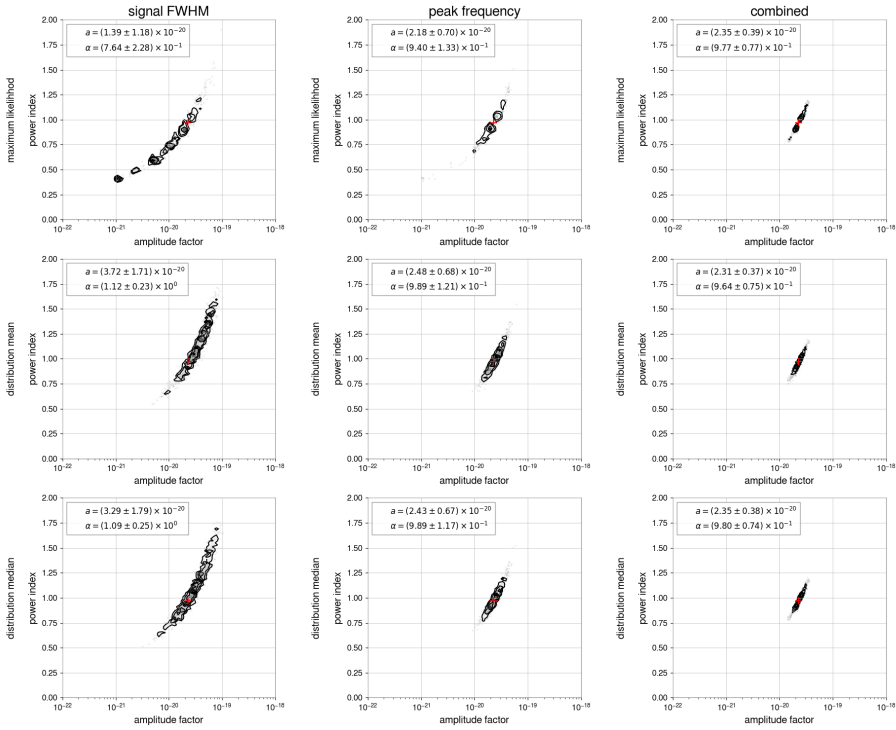


Figure 2.17: Comparison of the distributions of estimated parameters obtained via different methods. The first two columns use a single quantity, while the last one uses the combined method. The first row tries to use an optimizer to maximize the likelihood, while the last two use means and medians of the generated Markov chains.

CHAPTER 2. KNOW YOUR GLITCHES

Waiting for a glitch

In this chapter I will discuss how I simulated glitch occurrences. There are some observations on the waiting times predicted by the theory and what can be some more realistic expectations. A result that can be obtained is the estimation of a noise spectrum spoiled with little glitches.

3.1 Waiting times

Until now, the discussion was only about isolated glitches. A more complete description of the phenomenon involves a model that allows us to simulate the glitches timing.

3.1.1 Implementation

One can simply think that glitches will occur, like many phenomena, as a Poissonian process. But as affirmed in §1.4, this is not the case. To simulate them I use the dynamical system described in §1.4.2.

The generation of a burst sample starts from a random number drawn in the interval $[0, 1[$. This value represents the initial state of the system. The state is updated with the law 1.14. Examples of system evolutions are shown in Fig. 3.1.

Since we are only interested in the times at which the spikes are, at every iteration the old state (x_{n-1}) and the new (x_n) are compared to check if the threshold of 0.5 has been crossed in the ascending direction. If so, the iteration number n is appended to the list of spike times. The evolution of the system proceeds, discarding older states. When the list reaches a million spikes the simulation is stopped.

The height of the threshold will not influence the measured timing, since all the spikes have the same shape. This is valid until the threshold is set below the value \tilde{x} and above most of the injection values. If those conditions are respected, changing the threshold value will only add a constant shift to all the timings.

This process is repeated a hundred times for every couple of parameters, and all the lists of spike times are saved in files. In this way I will be able to generate samples long enough to contain a useful number of time windows to do some statistic.

3.1.2 Parameters of the bursts model

This system has two parameters: the *expansion coefficient* b and the *universality class* z .

The first regulates how fast is the rise of a burst signal. It also gives the scale of the problem, since it is correlated to the inverse of the iterations needed to have another spike. As a matter of fact, both the derivative of the continuous limit of the system and

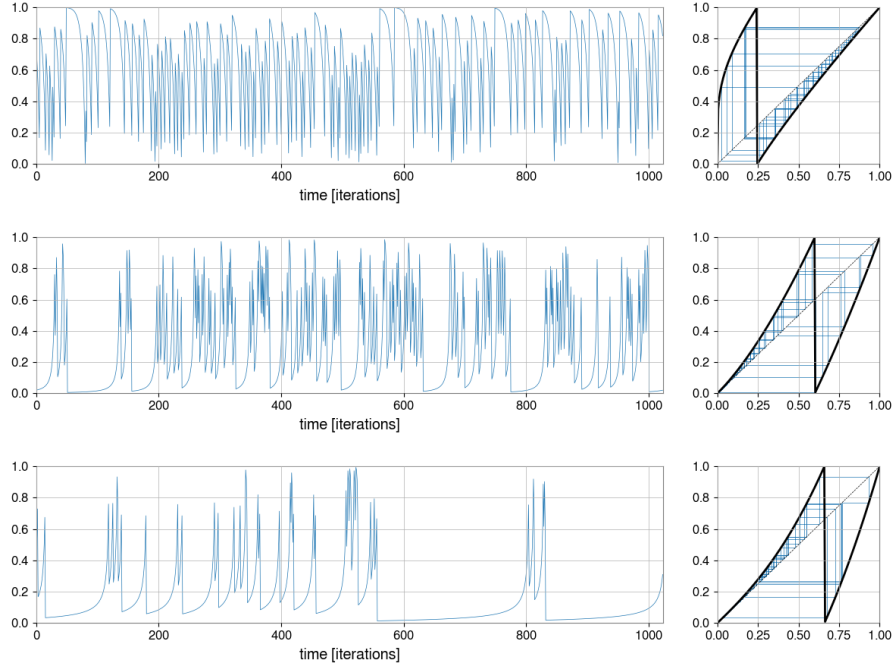


Figure 3.1: Samples generated with different combinations of burst parameters. In the first plot we can see how, a *universality class* under one flips the signal.

the duration of the intermissions show a dependence on this parameter.

The universality class is also correlated to those quantities, because it dictates the shape of a spike. Higher values of this parameter result in a spike with a greater curvature. Therefore, it will take a longer time to get to the maximum if we start from a smaller initial value, while the signal will continuously accelerate while ascending.

The *expansion coefficient* is bound in the interval $]0, 1[$, from the formulation of the dynamic system. The *universality class*, instead, is only limited to be a positive value different from one, so the interval of interest for it can only be found by exploring the parameter space. With high values of this parameter, the waiting times become larger and larger, until the model predicts very long periods of time without glitches. This can be used to limit the area to be explored.

The region that will be intensively studied is then defined for b and z by the respective intervals $10^{-3} \div 10^1$ and $0 \div 4$. Over the region a grid is defined with uniform spacing for the parameter z and uniform spacing, but in logarithmic space, for the other parameter.

3.1.3 Glitch probability

Like discussed in §2.3.2 not all real glitches can be utilized in an analysis, since some of them cannot be detected and others ones will be misidentified. Because of this, if we want to compare a generated distribution of waiting times with a real one, we must account this phenomenon.

A simple model can be made with the hypothesis of a constant probability of every glitch to be recognized, that does not depend on the previous glitches. This hypothesis seems to be reasonable, from the observation made in 1.2.3. To implement this, for every time contained in the saved lists I draw a random number to be compared with a threshold probability.

Since the probability of recognizing a glitch varies so much, I tried with ten different levels, equally spaced between 10% \div 100%. With this procedure, from every set of spike times generated from the dynamical system, I obtained ten different sets of possible glitch detection times.

After the generation of the filtered lists I computed the waiting times, subtracting from every time its predecessor. All the resulting lists are saved to a different file for every combination of parameters.

3.1.4 Waiting times shapes

After the whole procedure, I am ready to study the waiting times resulting from this simple model. To see how it behaves, I computed and plotted all the histograms from waiting times data.

We can observe how the shape changes with different combination of parameters: with low values of *expansion coefficients* and high *universality classes* the distribution is dominated by the power law.

With higher b the knee in the distribution recedes, until there is no power law left. In this regime the distribution become similar to an exponential. A subsample of the explored grid is shown in Fig. 3.2

All the shapes obtained with z under one are really similar to one another, with distributions all consisting of short times, so this seems an uninteresting region of parameter space. The reason for this similarity can be found in the shape of the function defining the dynamical system: with these values of the parameter z , the function will have an infinite derivative at $x = 0$, so the value of the variable will only get larger increments. These large increments will cause really fast ascends.

Instead, the descent will be ruled by the function that now is quasi-linear near one. This causes a slow descent, with spikes that appear flipped when compared with the ones that have a z parameter over one. We can see an example in Fig. 3.1. Those slow descents

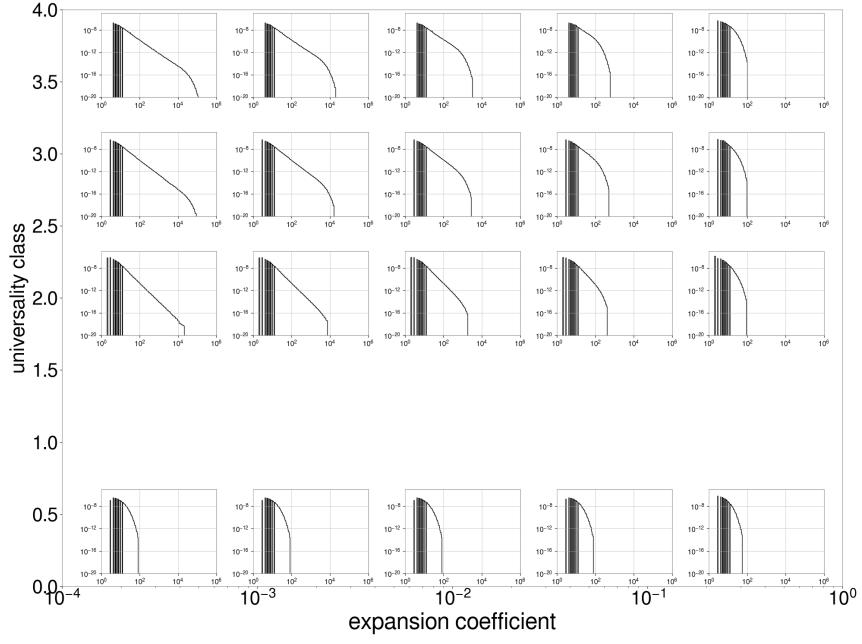


Figure 3.2: Distribution of waiting times in many points of the burst parameter space. The empty row is because the *universality class* parameter cannot be equal to one.

never reached a regime that led to a spikes distance longer than a hundred iterations.

With the addition of the chance to not detect all the glitches, the only thing that appear is a knee that for higher *universality classes* stays around the natural knee of the distribution, while for lower values it comes near the distribution peak. For these values of the parameter, the distributions seem to became independent of the parameter b . An example of this behavior is shown in Fig. 3.3.

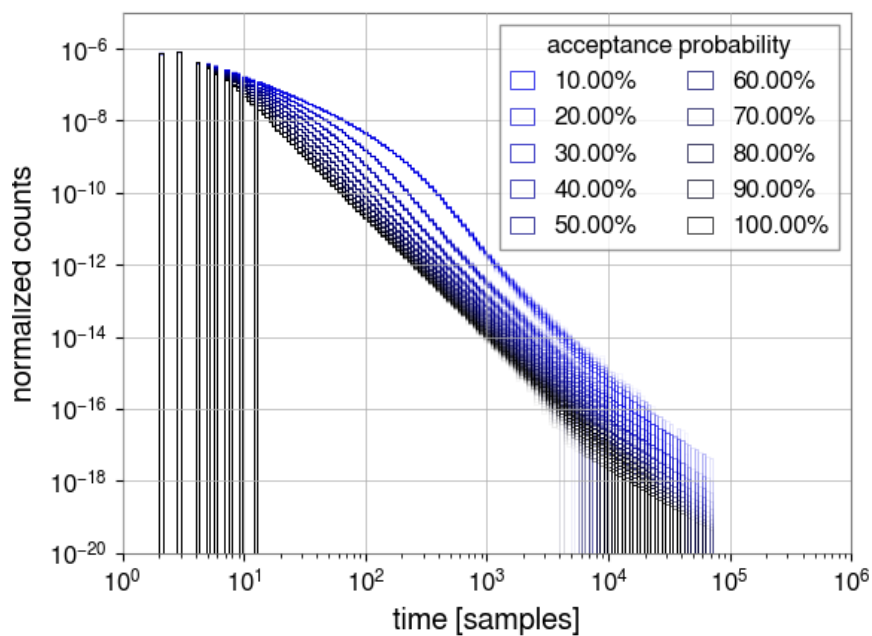


Figure 3.3: Example of how introducing the probability of not detect a glitch changes the shape of the waiting times distribution.

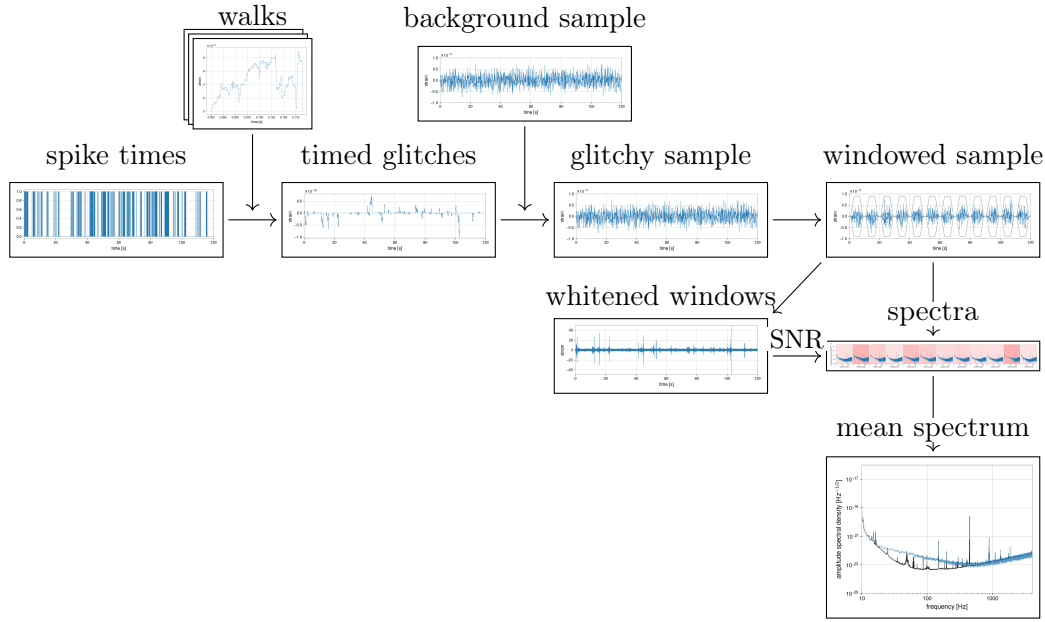


Figure 3.4: Workflow of the spectral modification analysis. The dynamic system is evolved for enough iterations to reach times that cover many time windows. The glitchy sample is then windowed, and for every window the spectrum is computed. Some louder segments are rejected if the corresponding SNR are too high. The result is a mean spectrum that can be confronted with the original ASD.

3.2 Spectral modification

An important result that we can obtain with a model for both the glitches and their timing is the contribution they make to the noise spectrum.

Since a fraction of glitches will always be too small to be detected, those glitches can be included in the quiet slices of strain selected to estimate the power noise of a detector, introducing also some non-Gaussianity to the noise statistic.

3.2.1 Glitch injection

To estimate the contribution of glitches to the amplitude spectral density of the detector I need a long sample with many glitches inside.

When I loaded one of the files with spike times from §3.1.1, I started iterating over the spikes. For every spike encountered I injected a glitch, if the spike did not happen in a time already covered by a glitch. In this way, the model works as a paralyzable detector, where the presence of a glitch excludes the start of another. This is because the glitches have already the chance to have a variable length, so the timing at short scales depends

on their intrinsic duration.

All those glitches are injected in an array of zeros, obtaining a sample with only glitches with the right timing.

I also generated a long background sample as described in §2.1.1. The length of the sample varies, as it is long enough to contain all the spikes for every spike set, with a margin of some seconds for the last glitch.

The background and the timed glitches are now ready to be analyzed.

3.2.2 Windowing

As stated in §1.2.1 the best way to have an estimation of the amplitude spectral density of the noise is to cut many windows of time, compute their spectra and take the average. I followed a similar procedure. The generated glitchy samples are divided in segments of ten seconds, shaped with a Planck-taper window[21].

From every window I compute the power spectral density of the small segment.

I defined five levels of SNR: $[3, 5, 7.5, 15, \infty]$. The last is chosen to check the contribution from all the glitches. For each one of them a control is made over the window: if the estimated SNR in the window is over the SNR threshold the spectrum is discarded and not used to compute the mean power spectral density of the glitchy sample. In this way we can study the effects of filtering glitches at many levels.

I applied the same procedure to the background sample, without SNR filtering, to have a control spectrum to be confronted with the glitchy spectra.

3.2.3 Spectral modification

With the illustrated procedure I studied a subsample of the quadri-dimensional grid that came by combining the two-dimensional ones described in §3.1.2 and §2.3.3. Two two-dimensional sections of the explored region is displayed in Fig. 3.5. In all the points where there was a glitch contribution to the spectra, the shape of the glitchy spectra was the same: a power law added to the instrumental power spectral density, with the same slope for all the combination of parameters.

The only thing that changes is the amplitude of the spectrum: with higher values of the *amplitude factor* a or smaller *expansion coefficient* b the contribution from the glitches is bigger.

We can also see in Fig. 3.6 how, in the one hundred runs I tested for every combination of parameters, the power law amplitude for the set that makes the mean of all the glitchy windows without limiting the SNR have a great variability.

A possible cause is that the mean is dominated by the loudest glitch of the sample, that

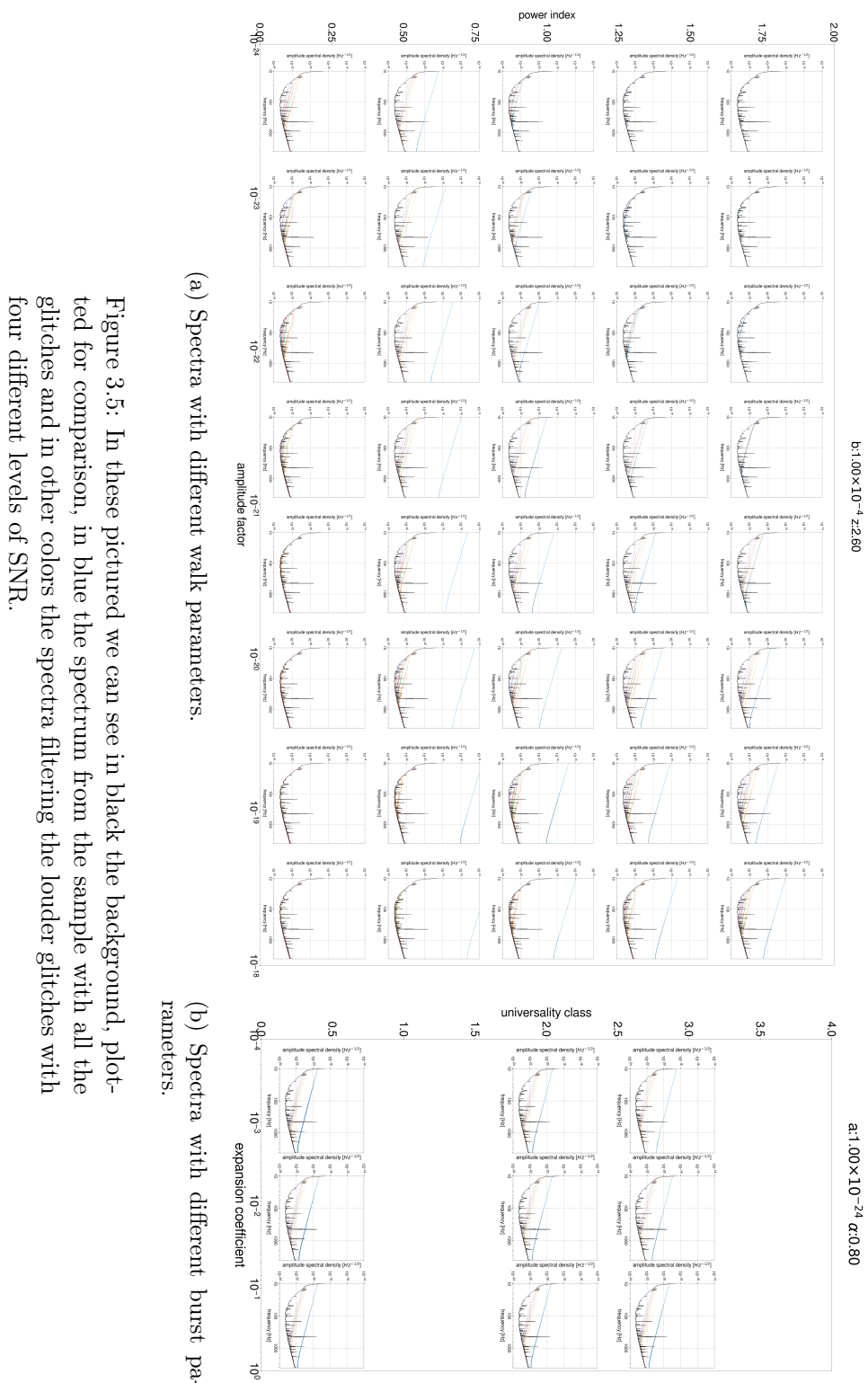


Figure 3.5: In these pictures we can see in black the background, plotted for comparison, in blue the spectrum from the sample with all the glitches and in other colors the spectra filtering the louder glitches with four different levels of SNR.

3.2. SPECTRAL MODIFICATION

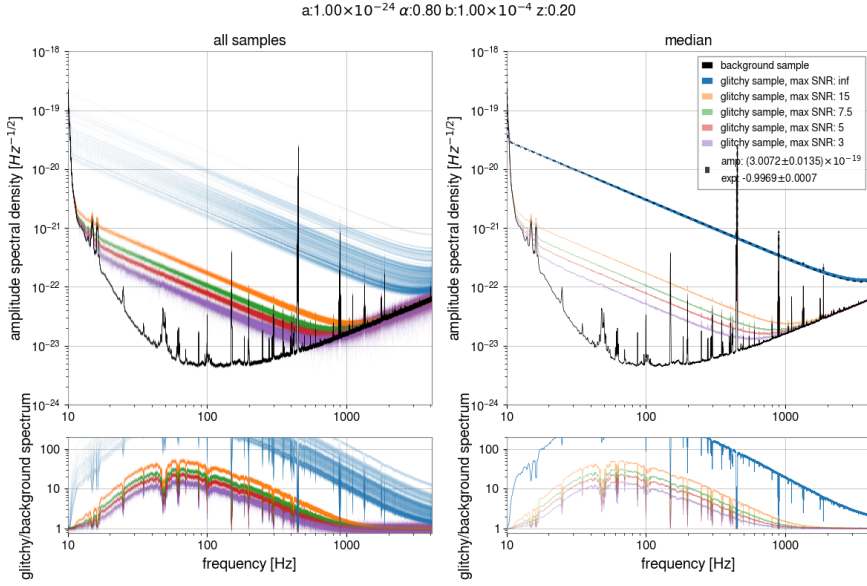


Figure 3.6: The spectra from the hundred runs made with one combination of parameters and the median spectrum. We can see how all the spectra have the same slope. We can also note that for in the set that retain all the glitches the variability of amplitude becomes important.

originates from a Lévy walk can be of many orders of magnitude bigger than the others. This kind of statistics makes the mean not converging, in fact to have a more stable estimation of the contribution to the amplitude spectral density I have taken the median of the hundred spectra.

To check if the slope really does not depend on the model parameters I fitted the amplitude spectral density that has the contribution from all the glitches with the formula:

$$ASD(f)^2 = ASD_{\text{detector}}(f)^2 + (mf^p)^2 + (m(f_{\max} - f)^p)^2 \quad (3.1)$$

that adds to the detector noise a power law of slope p and its mirrored version, to account the contribution from negative frequencies.

The results of this fit are shown in Fig. 3.7. We can see that almost all the powers are very close to -1 . The ones that differentiate from the others are the ones where almost all the glitches are too small to be observed, so the contribution is more difficult to estimate.



Figure 3.7: Power indices from the fit over the modified spectra. While always compatible with minus one, there are some deviations from the cases where the contribution is almost too small to be detected.

Conclusions and future prospects

In this thesis I studied a model that may explain some kind of glitches that affect the interferometers of the LIGO-Virgo-KAGRA Collaboration.

The model finds its foundation in the condensed matter theory that describes how ferromagnetic materials behave in presence of external magnetic fields. The Barkhausen effect describes how some small irregularities arise in the expected response of those materials. These fluctuations can be modeled as Lévy random walks, in a model that has two parameters.

Once produced, the pulses are hidden in generated samples of Gaussian noise with the same mean spectrum as the detector. The generated glitchy signals have been studied to check if they resemble real glitches. A first inspection is done using Q-scans, a way to represent signals in the time-frequency plane. In this way, many Gravity Spy classes can be successfully obtained: *blips, repeating blips, tomtes, koi fish, no glitch, extremely loud and none of the above*. I introduced two new categories, similar to some already existing, maybe due to slightly different plot procedures. The capability of generating many ratios in glitch population with different parameters may explain the variability in glitch proportions observed in different runs, when also the magnet population in the system is changed.

The glitches have been characterized with many different quantities that can be measured from the glitchy samples, like the *peak FWHM* or the *peak frequency*. In this quantity space different kinds of glitches show a high clustering, suggesting that these quantities can be a good way to study these events. The study of a large number of identified glitches also lead to a deeper understanding of their nature and the characteristics of every group.

These quantities have been used to prove that the random walk parameters can be inferred from a small set of generated glitches, in a procedure that can be also applied to real glitches.

I modeled the glitch timing, using the properties of a dissipative dynamical system to generate the observed bursts of events. I used this model to study the waiting times distributions, even with the chance of letting some glitches undetected.

One utility of this model is that it allows to estimate the contribution of glitches to the noise spectrum as one of the $1/f$ processes. This is valid, not only for the larger ones, but also for the smaller glitches that can pass undetected and contaminate noise.

The first thing that can be done in the future, is to find the distribution of the random walk parameters. Once they are found, they can be used to generate realistic glitches.

Thus, the generation of glitches can become systematic. A stable algorithm to generate glitches can be used to get training sets useful for machine learning programs that can do better glitch recognition and filtering.

Finally, since the model has a physical foundation, it identifies some detector components as possible culprits for this kind of noise. This may suggest actions to reduce noise events.

CHAPTER 4. CONCLUSIONS AND FUTURE PROSPECTS

Bibliography

- [1] B. P. Abbott et al. “Observation of Gravitational Waves from a Binary Black Hole Merger”. In: *Phys. Rev. Lett.* 116 (6 Feb. 2016), p. 061102. DOI: 10.1103/PhysRevLett.116.061102. URL: <https://link.aps.org/doi/10.1103/PhysRevLett.116.061102>.
- [2] Charles W Misner, Kip S Thorne, and John Archibald Wheeler. *Gravitation*. Macmillan, 1973.
- [3] Eric D. Black and Ryan N. Gutenkunst. “An introduction to signal extraction in interferometric gravitational wave detectors”. In: *American Journal of Physics* 71.4 (Apr. 2003), pp. 365–378. ISSN: 0002-9505. DOI: 10.1119/1.1531578. eprint: https://pubs.aip.org/aapt/ajp/article-pdf/71/4/365/10116606/365_1_online.pdf. URL: <https://doi.org/10.1119/1.1531578>.
- [4] T Accadia et al. “Virgo: a laser interferometer to detect gravitational waves”. In: *Journal of Instrumentation* 7.03 (Mar. 2012), P03012. DOI: 10.1088/1748-0221/7/03/P03012. URL: <https://dx.doi.org/10.1088/1748-0221/7/03/P03012>.
- [5] F. Acernese et al. “Measurements of Superattenuator seismic isolation by Virgo interferometer”. In: *Astroparticle Physics* 33.3 (2010), pp. 182–189. ISSN: 0927-6505. DOI: <https://doi.org/10.1016/j.astropartphys.2010.01.006>. URL: <https://www.sciencedirect.com/science/article/pii/S0927650510000253>.
- [6] T. Accadia et al. “A state observer for the Virgo inverted pendulum”. In: *Review of Scientific Instruments* 82.9 (Sept. 2011), p. 094502. ISSN: 0034-6748. DOI: 10.1063/1.3637466. eprint: https://pubs.aip.org/aip/rsi/article-pdf/doi/10.1063/1.3637466/16093120/094502_1_online.pdf. URL: <https://doi.org/10.1063/1.3637466>.
- [7] Hareem Tariq et al. “The linear variable differential transformer (LVDT) position sensor for gravitational wave interferometer low-frequency controls”. In: *Nuclear Instruments and Methods in Physics Research Section A: Accelerators, Spectrometers, Detectors and Associated Equipment* 489.1 (2002), pp. 570–576. ISSN: 0168-9002. DOI: [https://doi.org/10.1016/S0168-9002\(02\)00802-1](https://doi.org/10.1016/S0168-9002(02)00802-1). URL: <https://www.sciencedirect.com/science/article/pii/S0168900202008021>.
- [8] M Punturo et al. “The third generation of gravitational wave observatories and their science reach”. In: *Classical and Quantum Gravity* 27.8 (Apr. 2010), p. 084007. DOI: 10.1088/0264-9381/27/8/084007. URL: <https://dx.doi.org/10.1088/0264-9381/27/8/084007>.
- [9] B P Abbott et al. “A guide to LIGO–Virgo detector noise and extraction of transient gravitational-wave signals”. In: *Classical and Quantum Gravity* 37.5 (Feb. 2020), p. 055002. DOI: 10.1088/1361-6382/ab685e. URL: <https://dx.doi.org/10.1088/1361-6382/ab685e>.
- [10] S Chatterji et al. “Multiresolution techniques for the detection of gravitational-wave bursts”. In: *Classical and Quantum Gravity* 21.20 (Sept. 2004), S1809. DOI: 10.1088/0264-9381/21/20/024. URL: <https://dx.doi.org/10.1088/0264-9381/21/20/024>.

- [11] J. Timmer and M. König. “On generating power law noise.” In: A&A 300 (Aug. 1995), p. 707.
- [12] J Glanzer et al. “Data quality up to the third observing run of advanced LIGO: Gravity Spy glitch classifications”. In: *Classical and Quantum Gravity* 40.6 (Feb. 2023), p. 065004. DOI: 10.1088/1361-6382/acb633. URL: <https://dx.doi.org/10.1088/1361-6382/acb633>.
- [13] Florent Robinet et al. “Omicron: A tool to characterize transient noise in gravitational-wave detectors”. In: *SoftwareX* 12 (2020), p. 100620. ISSN: 2352-7110. DOI: <https://doi.org/10.1016/j.softx.2020.100620>. URL: <https://www.sciencedirect.com/science/article/pii/S2352711020303332>.
- [14] Robert C O’Handley. *Modern magnetic materials*. en. Nashville, TN: John Wiley & Sons, Nov. 1999.
- [15] James P. Sethna, Karin A. Dahmen, and Christopher R. Myers. “Crackling noise”. In: *Nature* 410.6825 (Mar. 2001), pp. 242–250. ISSN: 1476-4687. DOI: 10.1038/35065675. URL: <https://doi.org/10.1038/35065675>.
- [16] George H. Weiss. “A Primer of Random Walkology”. In: *Fractals in Science*. Ed. by Armin Bunde and Shlomo Havlin. Berlin, Heidelberg: Springer Berlin Heidelberg, 1994, pp. 119–162. ISBN: 978-3-642-77953-4. DOI: 10.1007/978-3-642-77953-4_5. URL: https://doi.org/10.1007/978-3-642-77953-4_5.
- [17] Andrea Baldassarri, Francesca Colaiori, and Claudio Castellano. “Average Shape of a Fluctuation: Universality in Excursions of Stochastic Processes”. In: *Phys. Rev. Lett.* 90 (6 Feb. 2003), p. 060601. DOI: 10.1103/PhysRevLett.90.060601. URL: <https://link.aps.org/doi/10.1103/PhysRevLett.90.060601>.
- [18] Manneville, P. “Intermittency, self-similarity and 1/f spectrum in dissipative dynamical systems”. In: *J. Phys. France* 41.11 (1980), pp. 1235–1243. DOI: 10.1051/jphys:0198000410110123500. URL: <https://doi.org/10.1051/jphys:0198000410110123500>.
- [19] Duncan Macleod et al. *gwp/gwp: GWpy 3.0.9*. Version v3.0.9. July 2024. DOI: 10.5281/zenodo.12734623. URL: <https://doi.org/10.5281/zenodo.12734623>.
- [20] Daniel Foreman-Mackey et al. “emcee: The MCMC Hammer”. In: *Publications of the Astronomical Society of the Pacific* 125.925 (Feb. 2013), p. 306. DOI: 10.1086/670067. URL: <https://dx.doi.org/10.1086/670067>.
- [21] “Bump Functions and Partitions of Unity”. In: *An Introduction to Manifolds*. New York, NY: Springer New York, 2008, pp. 127–134. ISBN: 978-0-387-48101-2. DOI: 10.1007/978-0-387-48101-2_13. URL: https://doi.org/10.1007/978-0-387-48101-2_13.